Coastal Engineering 157 (2020) 103648

Contents lists available at ScienceDirect

Coastal Engineering

journal homepage: http://www.elsevier.com/locate/coastaleng

Experimental study on vegetation flexibility as control parameter for wave damping and velocity structure

Thomas J. van Veelen [a,*], Tom P. Fairchild [b], Dominic E. Reeve [a], Harshinie Karunarathna [a]

[a] Energy and Environment Research Group, Zienkiewicz Centre for Computational Engineering, Swansea University, Swansea, United Kingdom
[b] School of Biosciences, Swansea University, Swansea, United Kingdom

ARTICLE INFO

Keywords:
Salt marsh vegetation
Wave damping
Plant flexibility
PIV-Measurements
Flow velocities

ABSTRACT

Vegetation can contribute to coastal defence by damping incoming waves. However, prior studies have shown that attenuation varies greatly among plant species. Plant flexibility is a mechanical property that is commonly omitted, but varies considerably between shrubs and grasses on salt marshes. Therefore, we present an experimental study in a laboratory wave flume with artificial vegetation that differs in flexibility only. We measured wave attenuation and water particle velocities around rigid and flexible salt marsh vegetation. Waves were measured using a series of gauges and Particle Image Velocimetry (PIV) was used to measure spatio-temporal variations of water particle velocities in the *x*-*z* plane around the vegetation. Our results show that flexible vegetation attenuates waves up to 70% less than rigid vegetation due to swaying of flexible plants. Furthermore, we find that rigid vegetation modifies the velocity structure, whereas flexible vegetation does not. Specifically, a mean current in the direction of wave propagation develops around the canopy and the horizontal particle velocities are amplified directly above the canopy. These results indicate that plant flexibility is a key parameter in the wave-vegetation interaction that controls wave damping and velocity structure.

1. Introduction

Nature-based coastal defences in the form of vegetated foreshores are increasingly common in coastal protection schemes. The vegetation reduces the wave impact on natural beaches and coastal defence structures (Leonardi et al., 2018; Möller et al., 2014; Temmerman et al., 2013) and mitigates the impacts of storm surges (Wamsley et al., 2009). At the same time, they enhance natural habitats (Nordstrom, 2014), provide recreational opportunities (Foster et al., 2013), and act as a grazing area for cattle (Davidson et al., 2017).

Salt marshes are vegetated tidal wetlands that can be part of a nature-based coastal defence solution. The potential of their vegetation to damp waves has been shown in the field (Jadhav et al., 2013) and in large-scale experiments (Losada et al., 2016; Möller et al., 2014). Furthermore, they capture and bind sediments (Fagherazzi et al., 2012), which contributes to coastal stability (Bouma et al., 2014) and provides adaptation to sea level rise (French, 1993).

In an attempt to quantify the impact of vegetation on wave attenuation, computational modellers have proposed different approaches. Price et al. (1968) used a high viscous layer to model the impact of submerged seaweed. This approach was later extended by Mork (1996), who also included form drag from the canopy and near the substrate. Alternatively, Camfield (1983) studied the impact of vegetation on wind-driven wave growth via an enhanced bottom drag coefficient. Recent modelling studies have used this simple approach to simulate vegetation impacts on waves and storm surges (Stark et al., 2016; Wamsley et al., 2009). However, both approaches require additional formulations to relate plant properties to viscosity and bottom drag respectively.

Using an alternative approach, Dalrymple et al. (1984) developed a direct relationship for wave attenuation as a function of wave and vegetation parameters. By simplifying the plant geometry to rigid cylinders and assuming the validity of linear wave theory (see e.g. Dean and Dalrymple, 1991 for details), a uniform bed and monochromatic wave trains, they quantified losses in wave energy due to work done by the drag force on the vegetation. Ultimately, they showed that this resulted in a reciprocal decay in wave height over a vegetation field.

Mendez and Losada (2004) expanded on Dalrymple et al. (1984) by introducing new relations for random sea states and bed slope effects. Furthermore, they validated their work with kelp experiments by Dubi (1997). They showed that the bulk drag coefficient C_D, hereinafter referred to as drag coefficient, is key in predicting wave attenuation by

* Corresponding author.
E-mail address: t.j.van-veelen.922560@swansea.ac.uk (T.J. van Veelen).

https://doi.org/10.1016/j.coastaleng.2020.103648
Received 21 February 2019; Received in revised form 12 December 2019; Accepted 19 January 2020
Available online 24 January 2020

vegetation, because it is the only parameter that cannot be readily measured in the field and depends on the hydrodynamic conditions. It was shown that its value was inversely related to the Keulegan Carpenter number (KC; Mendez and Losada, 2004). Yet, the results cannot be easily expanded to other studies, because the drag coefficient also acts as a calibration parameter that compensates for the assumptions made, such as the simplification of the plant geometry.

The framework as set out by Dalrymple et al. (1984) and Mendez and Losada (2004) has been successfully applied in experiments with artificial and real salt marsh vegetation to obtain additional relations for the drag coefficient. For example, Jadhav et al. (2013) confirmed an inverse relation between the *KC* number and the drag coefficient based on measurements on a *Spartina Alterniflora* marsh. Alternatively, the drag coefficient has been related to the vegetation Reynolds number *Re* in experimental studies. This includes experiments with vegetation mimics, using a variety of materials, plant shapes and plant dimensions (Anderson and Smith, 2014; Augustin et al., 2009; Chen et al., 2018; Hu et al., 2014; Koftis et al., 2013; Ozeren et al., 2014; Phan et al., 2019), as well as experiments with real vegetation such as *Puccinellia Maritima* and *Elymus Athericus* (Möller et al., 2014) and *Puccinellia Maritima* and *Spartina Anglica* (Lara et al., 2016; Losada et al., 2016). Regardless of whether *KC* or *Re* is used, all studies found a reduction in drag coefficient for increased orbital wave particle velocities which are associated with higher waves.

However, a comparison by Vuik et al. (2016) revealed that for hydrodynamic conditions typical for a salt marsh, drag coefficients ranged from 0.13 to 5.75, which differ by a factor of 44. This indicates that hydrodynamic conditions are not a sufficient predictor for the drag coefficient. Submergence ratio (Anderson and Smith, 2014; Garzon et al., 2019; Mendez and Losada, 2004) and biomass (Maza et al., 2015) have been studied, but results are not consistent among experiments and both parameters are accounted for in the framework by Dalrymple et al. (1984) and Mendez and Losada (2004). This suggests that other parameters may be important.

Recently, Paul et al. (2016) have shown that plant flexibility may affect the potential of vegetation to attenuate waves, particularly when orbital velocities are low. Although their results have been obtained using a small quantity (max 8) of rectangular Lexaan strips instead of a full vegetation meadow, it has drawn attention to the potential importance of flexibility which varies greatly among plant species (Chatagnier, 2012). These observations are supported by the low drag coefficients reported in studies with flexible grasses (e.g. Möller et al., 2014). Furthermore, numerical modelling exercises have shown that plant swaying reduces the drag forces on flexible vegetation (Luhar and Nepf, 2016; Méndez et al., 1999; Mullarney and Henderson, 2010). However, Augustin et al. (2009) found no difference between rigid and flexible mimics. Therefore, additional research is needed on how plant flexibility affects wave attenuation.

Experimental results have also challenged the assumption that the velocity structure follows linear wave theory in the presence of vegetation. For instance, the orbital velocities were preferentially attenuated within meadows of wide rigid cylinders (Lowe et al., 2005; Pujol et al., 2013) and flexible vegetation (Luhar et al., 2010; Rupprecht et al., 2017). Furthermore, wave-averaged net currents were observed around artificial rigid (Abdolahpour et al., 2017; Hu et al., 2014; Pujol et al., 2013) and flexible (Abdolahpour et al., 2017; Luhar et al., 2010) vegetation patches. These modifications in the velocity structure directly impact the magnitude of the drag force and the work done by it.

However, the magnitude of velocity attenuation and the direction and position of net currents differ between rigid and flexible vegetation. In an experiment with artificial rigid and flexible vegetation under equal wave conditions, Pujol et al. (2013) identified velocity attenuation by rigid vegetation only. Furthermore, rigid vegetation induces net currents in the direction of wave propagation through the top of the vegetation (Pujol et al., 2013) and flexible vegetation near the bottom (Luhar et al., 2010; Rupprecht et al., 2017).

Thus, plant flexibility may also be a key predictor for changes in wave-driven velocities, but much remains unclear in the absence of high-quality comparative data. Rigid and flexible vegetation with identical shapes have not yet been tested. Cylinders were used to mimic rigid vegetation (Abdolahpour et al., 2017; Hu et al., 2014; Lowe et al., 2005; Pujol et al., 2013) as opposed to blades (Abdolahpour et al., 2017; Luhar et al., 2010; Pujol et al., 2013) or real grasses (Rupprecht et al., 2017) for flexible vegetation. Furthermore, measurements have been restricted to points (Hu et al., 2014; Rupprecht et al., 2017) or cross-sections (Abdolahpour et al., 2017; Lowe et al., 2005; Luhar et al., 2010; Pujol et al., 2013). Full velocity fields have not been measured yet.

Therefore, we tested wave attenuation by and the velocity structure around rigid and flexible vegetation meadows that differ in flexibility only. Plant parameters and wave conditions were directly derived from salt marshes in South Wales, UK to mimic realistic plant properties for this study. The salt marshes in South Wales exhibit diverse vegetation with large variation in plant stem flexibility, which is important to this study. As a further key element, Particle Image Velocimetry (PIV) is used to measure the velocity structure in the *x*-*z* plane around vegetation.

2. Theoretical background

Let us define a coordinate system (Fig. 1), where the *x*-axis is in the direction of wave propagation with $x = 0$ at the front edge and $x = L_v$ at the back edge of the vegetation. Furthermore, the *z*-axis describes the vertical position with respect to the water column such that $z = 0$ depicts the still water surface and $z = -h$ the bed level. Herein, waves travel over a flat bottom with a vegetation field. Following Dalrymple et al. (1984), plant geometry is simplified to rigid upright cylinders with height h_v, diameter b_v and spacing S_v, such that $S_v = n_v^{-0.5}$ with n_v as the stem density in stems/m^2. Furthermore, sinusoidal waves with height $H(x)$ and period T are imposed on the domain.

When waves travel over vegetation fields, energy is dissipated due to the work done by the waves on the plants (Dalrymple et al., 1984). A time-averaged wave dissipation constant per unit horizontal area is defined as

$$\varepsilon_v = \overline{\int_{-h}^{-h+h_v} \boldsymbol{F}\boldsymbol{u} dz}. \tag{1}$$

$\varepsilon_v = -c_g \partial E/\partial x$ is the wave dissipation constant where $c_g = \frac{\omega}{2k}\left(1 + \frac{2kh}{\sinh 2\,kh}\right)$ is the wave group velocity and $E = \rho g H^2/8$ is the wave energy. Herein, ω is the wave angular frequency, k is the wave number, $\rho = 1000$ kg/m^3 is the density of water, and $g = 9.81$ m/s^2 is the gravitational acceleration. Furthermore, $\boldsymbol{F} = (F_x, F_z)$ is the force exerted by the waves on the vegetation per unit volume and $\boldsymbol{u} = (u, w)$ is the local flow velocity. The horizontal component of the wave force is typically considered dominant i.e. $\boldsymbol{F}\boldsymbol{u} \approx F_x u$ (Kobayashi et al., 1993; Méndez et al., 1999). F_x is given by a Morison type equation (Morison et al., 1950), according to

$$F_x = \frac{1}{2}\rho C_D b_v n_v |u_r| u_r + \frac{\pi}{4}\rho C_M b_v^2 n_v \frac{\partial u_r}{\partial t} \tag{2}$$

where u_r is the relative velocity between water and vegetation, C_D is the drag coefficient, and C_M is the inertia coefficient. The effect of vegetation motion is considered through calibration of the drag coefficient (Mendez and Losada, 2004; Möller et al., 2014). Additionally, the contribution of the drag term is expected to exceed the contribution of the inertia term with respect to wave attenuation because the inertia term acts out of phase with the velocity (Dalrymple et al., 1984; Kobayashi et al., 1993; Mendez and Losada, 2004). Under these conditions, the wave force reduces to

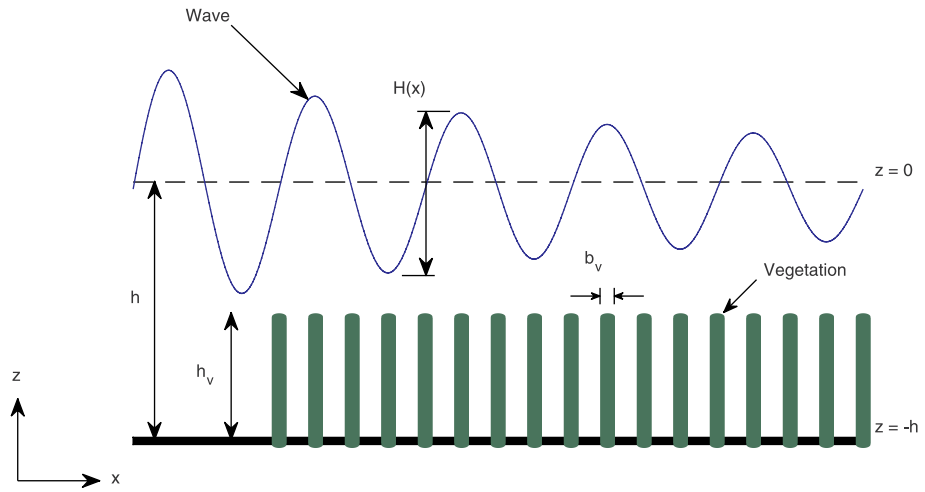

Fig. 1. Schematisation of wave attenuation over vegetation.

$$F_x = \frac{1}{2}\rho C_D b_v n_v |u| u. \tag{3}$$

Further assuming validity of linear wave theory, Dalrymple et al. (1984) showed that waves decay reciprocally with distance across vegetation, according to

$$H(x) = \frac{H_0}{1+\beta x}\ , \tag{4}$$

with

$$\beta = \frac{4}{9\pi} C_D b_v n_v H_0 k \frac{\sinh^3 k\alpha h + 3\sinh k\alpha h}{(\sinh 2\,kh + 2kh)\sinh kh}\ . \tag{5}$$

Herein, H_0 is the wave height at the front edge of the vegetation field, β is the wave damping coefficient, and $\alpha = \frac{h_v}{h}$ is the submergence ratio. According to Eq. (5), the magnitude of the wave damping coefficient is a function of vegetation properties, flow conditions and the drag coefficient. Importantly, the drag coefficient implicitly acts as a calibration parameter for the assumptions made. The default value of C_D for rigid cylinders is therefore not applicable.

3. Experimentation

3.1. Flume setup

Experiments with rigid and flexible plant mimics were conducted in the wave flume of the Coastal Laboratory of Swansea University, UK. The flume is 30.7 m in length, 0.8 m in width and 1.2 m in height. It has glass side walls and a metal bottom. The flume has a piston type wavemaker with active wave absorption at one end and a parabolic wave damper of reticulated foam at the other end (Fig. 2a).

Rigid and flexible vegetation mimics were fixed on the flume floor. The rigid vegetation was created from bamboo dowels ($\rho_v = 350$ kg/m^3; Fig. 2b) and flexible vegetation from silicon sealants ($\rho_v = 998$ kg/m^3;

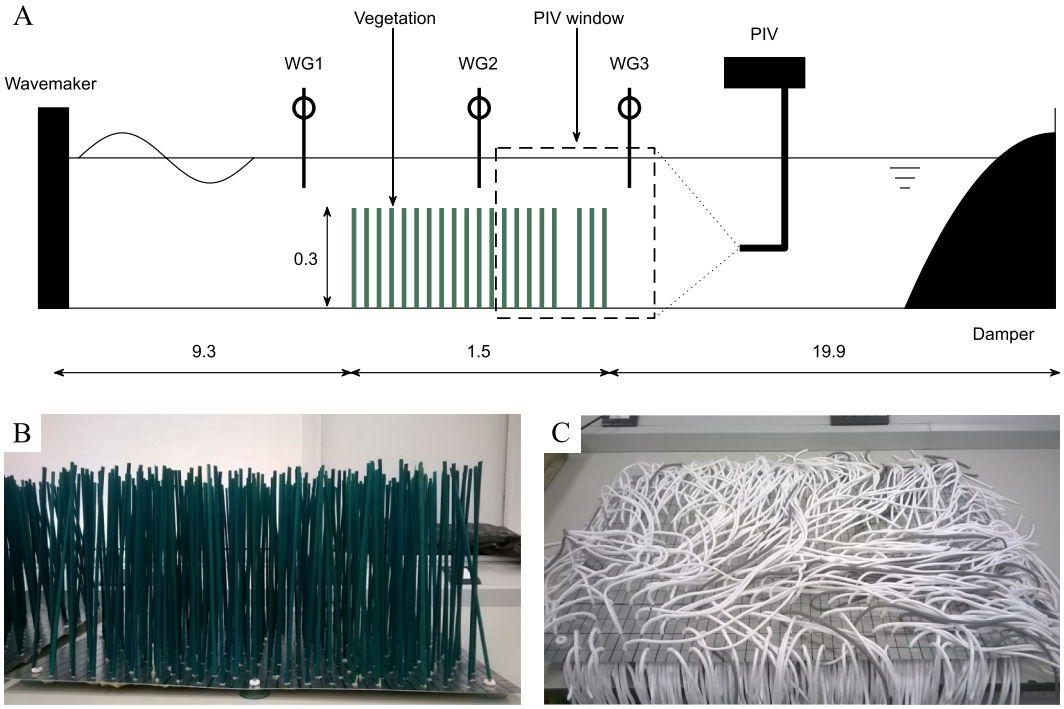

Fig. 2. (a) Sketch of the experimental set-up. All dimensions are in metres. Figure is not to scale; (b) Artificial rigid vegetation; (c) Artificial flexible vegetation.

Fig. 2c). The two plant mimics differed in flexural rigidity, $EI = 9.0 \pm 4 \times 10^{-2}$ Nm^2 for the dowels and $EI = 1.7 \pm 0.3 \times 10^{-5}$ Nm^2 for the sealants. Both vegetation types were cylinders with a diameter of 5 mm and a height of 300 mm. They were fitted into aluminium plates (500 mm long, 750 mm wide, 0.9 mm thick) with pre-drilled holes. The holes were aligned in a series of rows normal to the wave direction. The spacing between rows was 30 mm and the spacing between stem centres on a row were 30 mm for a stem density of 1111 stems/m^2. However, subsequent rows had a lateral shift of 15 mm to obtain a staggered grid which resembles the scattering of real vegetation.

The vegetation plates were attached to the flume floor by suction cups at the plate centres, corners and edge centres. They attached well to the floor with minimum separation between plate and flume floor. Three rigid and flexible vegetation plates were constructed for a total vegetation length of 1.5 m. Following Luhar et al. (2010) and Pujol et al. (2013), two rows of vegetation were removed to create a 90 mm gap to enable PIV measurements within the plant meadow. It is assumed that the orbital water particle motion within this gap will not differ from its surroundings, which is validated by repeating each run without a gap in the vegetation.

Three wave gauges (WG1, WG2 & WG3) and a PIV system (Dantec Systems) were installed to measure the wave-induced variations in water surface elevation and particle velocity (Fig. 2a). WG1 was placed 1.05 m upstream of the vegetation patch, WG2 was placed central in the patch, and, finally, WG3 was placed 0.10 m downstream of the vegetation. Furthermore, a laser inside the flume and a camera on the side were the main components of the PIV system to measure the water particle velocities. The laser was placed 2–3 m downstream of the vegetation patch. Its exact location was optimised for each water depth. Details about wave attenuation and particle velocity measurements are provided in Sections 3.4 and 3.5 respectively.

Despite the presence of a wave damper at the end of the flume, the impact from wave reflection was significant. Therefore, only the time window unaffected by reflected waves was used in the data analysis. This was defined as the period between full wave development and the return of the first reflected wave to WG3 (Möller et al., 2014). Waves were considered fully developed when the water level reached 95% of the incident wave amplitude and at least five waves had passed. The return time was derived from shallow water wave theory. Four to eleven waves fell within the curtailed frame, depending on wave period and water depth. Therefore, each condition was run three times to obtain sufficient data: two times with a gap in the vegetation and one run without a gap.

3.2. Wave conditions

The rigid and flexible vegetation patches were subjected to 24 regular wave conditions (Table 1). Specifically, the wave height varied between 0.08 and 0.20 m, the wave period between 1.4 and 2.0 s, and the water depth between 0.60 and 0.30 m. A velocity scale, U, is defined as the maximum orbital velocity at stem centre ($z = -h + 1/2h_v$) in front of the vegetation ($x = 0$) based on linear wave theory. Each condition was run three times for both vegetation types. Finally, control runs without vegetation were conducted for cases R3, R13, R23 and R33. Videos of the experiments under conditions R13 and R23 are included as supplementary material in the Web version of this manuscript.

3.3. Experiment similarity

Past studies (see Vuik et al., 2016 for a review) have shown that drag coefficient relationships for wave attenuation strongly rely on hydrodynamic and vegetation conditions. It is important that selected experimental conditions represent field conditions. Therefore, the experimental conditions in this study are supported by plant data from two field campaigns in South Wales estuaries, and wave data from a concurrent numerical modelling study of wave penetration in a sheltered macrotidal estuary (Bennett et al., pers. comm.), which is typical for South Wales. Details are provided in Appendix A.

There is no scale difference between field and flume, but it remains key to verify that the wave-vegetation interactions are similar. Four components control this interface: (i) the plant dimensions, (ii) the incoming wave dynamics, (iii) the hydrodynamic impact on the waves by the vegetation, and (iv) the response of the plants to the orbital wave motion (plant swaying). A detailed list of parameters and ratios is provided in Table 2.

First, the dimensions h_v, b_v and n_v of the vegetation mimics are within the range typical for South Wales salt marshes. Furthermore, the relative share of vegetation in the water column is expressed by the submergence ratio $\alpha = \frac{h_v}{h}$ (e.g. Augustin et al., 2009; Koftis et al., 2013) and relative stem frontal area $\lambda_f = h_v b_v n_v$. The conditions considered in

Table 1
List of tested wave conditions. Each condition was tested three times with rigid and flexible vegetation.

Case	Wave type	H [m]	T [s]	h [m]	U [m/s]	KC	L	F_r	Re	Ca (rigid vegetation)	Ca (flexible vegetation)
R1	Regular	0.15	1.4	0.60	0.19	53	7.13	0.08	945	0.053	279
R2	Regular	0.15	1.6	0.60	0.22	69	5.47	0.09	1077	0.069	362
R3	Regular	0.15	1.8	0.60	0.23	84	4.48	0.10	1169	0.082	427
R4	Regular	0.15	2.0	0.60	0.25	99	3.82	0.10	1235	0.091	476
R5	Regular	0.10	1.8	0.60	0.16	56	6.72	0.06	779	0.036	190
R6	Regular	0.20	1.8	0.60	0.31	112	3.37	0.13	1559	0.145	755
R11	Regular	0.15	1.4	0.50	0.23	65	5.80	0.10	1160	0.081	421
R12	Regular	0.15	1.6	0.50	0.26	82	4.61	0.12	1277	0.098	510
R13	Regular	0.15	1.8	0.50	0.27	98	3.85	0.12	1358	0.111	576
R14	Regular	0.15	2.0	0.50	0.28	113	3.34	0.13	1416	0.120	623
R15	Regular	0.10	1.8	0.50	0.18	65	5.78	0.08	906	0.049	256
R16	Regular	0.20	1.8	0.50	0.36	130	2.90	0.16	1811	0.195	1018
R21	Regular	0.15	1.4	0.40	0.29	81	4.65	0.15	1447	0.125	653
R22	Regular	0.15	1.6	0.40	0.31	99	3.82	0.16	1544	0.143	744
R23	Regular	0.15	1.8	0.40	0.32	116	3.25	0.16	1610	0.156	810
R24	Regular	0.15	2.0	0.40	0.33	133	2.83	0.17	1658	0.166	863
R25	Regular	0.10	1.8	0.40	0.21	77	4.88	0.11	1074	0.069	360
R26	Regular	0.12	1.8	0.40	0.26	93	4.06	0.13	1288	0.100	519
R31	Regular	0.10	1.4	0.30	0.25	70	5.42	0.14	1242	0.093	482
R32	Regular	0.10	1.6	0.30	0.26	82	4.58	0.15	1287	0.099	517
R33	Regular	0.10	1.8	0.30	0.26	95	3.98	0.15	1317	0.104	541
R34	Regular	0.10	2.0	0.30	0.27	107	3.52	0.16	1339	0.107	558
R35	Regular	0.08	1.8	0.30	0.21	76	4.97	0.12	1054	0.067	347
R36	Regular	0.12	1.8	0.30	0.32	114	3.31	0.18	1580	0.150	783

Table 2
List of parameter values for field and experiment conditions. It is divided in sections plant data (top), wave data (middle) and dimensionless ratios (bottom).

Parameter	Symbol	Field (S. Wales)	Rigid mimics	Flexible mimics	Unit
Stem height	h_v	231–590	300	300	mm
Stem diameter	b_v	0.74–5.50	5	5	mm
Stem density	n_v	214–2275	1111	1111	m^{-2}
Young's modulus	E	139–2343	2917	0.56	MPa
Flexural rigidity	EI	1.9×10^{-5} – 2.6×10^{-2}	9.0×10^{-2}	1.7×10^{-5}	Nm^2
Bulk density[a]	ρ_v	N/A	350	998	kgm^{-3}
Water depth	h	0–0.6	0.30–0.60	0.30–0.60	m
Wave height	H	0.1–0.2	0.08–0.20	0.08–0.20	m
Wave period	T	2.0	1.4–2.0	1.4–2.0	s
Velocity scale	U	0.17–0.33	0.16–0.36	0.16–0.36	m/s
Submergence ratio	α	0.39–1.0	0.5–1.0	0.5–1.0	–
Relative frontal area	λ_f	0.57–6.10	1.67	1.67	–
Froude number[b]	F_r	0.10	0.10	0.10	–
Reynolds number[b]	Re	185–1375	1250	1250	–
Keulegan-Carpenter number[b]	KC	91–676	100	100	–
Cauchy number[b]	Ca	1.55–103	0.09	488	–
Excursion ratio[b]	L	2.90–7.41	3.77	3.77	–

[a] All field vegetation was observed to be buoyant, but the exact bulk densities could not be measured accurately with the available equipment.
[b] Reference hydrodynamic conditions: $H = 0.15$ m, $T = 2$s, $U = 0.25$ m/s.

this study, $\alpha = 0.50$–1.0 and $\lambda_f = 1.67$, are within the range of field conditions.

Second, the incoming wave conditions have been selected within the range of numerical modelling results. These served as direct input to the wavemaker. Therefore, key ratios such as the Froude number $F_r = U/\sqrt{gh}$ (e.g. Bullock et al., 2001) and the relative wave height $H_r = H/h$ are automatically satisfied among field and experiment conditions.

Third, the hydrodynamics around salt marsh plants are controlled by the wake structures induced by the vegetation, expressed by vegetation Reynolds Number $Re = Ub_v/\nu$ (e.g. Nepf, 1999), in which ν is the kinematic viscosity. Alternatively, the Keulegan-Carpenter number $KC = UT/b_v$, which is effectively a ratio between wave excursion and stem diameter, has been identified as a predictor for the drag coefficient on cylinders (Keulegan and Carpenter, 1958). Re and KC fall within the range of field conditions (Table 2). Specifically, Re varies from 779 to 1811 and KC varies between 53 and 133 depending on test conditions (Table 1).

Fourth, plant swaying is induced by wave forcing on flexible vegetation. Luhar and Nepf (2016) showed that plant swaying under vegetation is controlled by the Cauchy Number $Ca = \rho b_v U^2 h_v^3/EI$ as the ratio of drag force over restoring forces due to stiffness, and the excursion ratio $L = h_v/A_w$ as the ratio between stem length over water particle excursion $A_w = UT/(2\pi)$. Buoyancy may delay the onset of plant bending but is not expected to affect wave dynamics when wave forcing is significant (large Ca) (Henderson, 2019; Luhar et al., 2017; Luhar and Nepf, 2016, 2011). The Cauchy numbers of rigid ($Ca =$ 0.04–0.20) and flexible ($Ca =$ 200–1000) mimics cover the range of real vegetation in South Wales ($Ca = 1.55$–103) and those reported in the literature (e.g. Rupprecht et al., 2017 reported $Ca =$ 0.3-1000 for *E. Athericus* and *P. Maritima*). Also, the excursion ratio matches well with $L = 2.83$– 7.13 in the experiments, compared to $L =$ 2.90–7.41 in the field.

3.4. Wave attenuation measurements

The wave attenuation parameter β is obtained from the energy spectra that are derived from wave gauges in front of (WG1), halfway (WG2), and after (WG3) the artificial vegetation patch (Fig. 2a). Measured water surface elevation time series were curtailed to the maximum number of fully developed waves within the timeframe unaffected by reflection. We corrected for phase differences between each gauge in this process to obtain equivalent time series. These were used to calculate the wave energy spectra and, subsequently, zeroth spectral moment wave height $H_{m,0}$ at each gauge.

The zeroth spectral moment wave height was previously successfully applied for irregular waves by Koftis et al. (2013) and Anderson and Smith (2014) and was preferred over zero up-crossing, because the nonlinear interactions in shallow water induced higher order harmonics. Furthermore, this concept is consistent with the attenuation in wave energy as described in Section 2.

The three runs for each test condition were combined, and a single β was fitted to Eq. (4) using the least squares method (Fig. 3). Then, the associated drag coefficient C_D can be obtained via Eq. (5). The control experimental runs without vegetation showed that the contribution of bottom friction to wave damping did not affect the results ($\beta < 0.005$).

3.5. Wave particle velocity measurements

Water particle velocities over, after and within the vegetation were measured using Particle Image Velocimetry (PIV; Dantec Systems). Polyamid seeding particles that follow water particle motion are added to the flume. By shooting two frames of the particle positions, their velocity can be calculated from their movement in between the pair of frames. Crucially, the pairing frames are shot with minimal time difference, here 2 ms; illumination in the *x*-*z* plane is provided by a laser and images are shot by a high-resolution camera through the glass walls of the flume.

The laser (Nano L 100–50 PIV, Litron Lasers) was placed inside the water column downstream of the vegetation patch to avoid interference with the wave motion. The camera (Speedsense 1040) placement and zoom were adjusted to maximize resolution whilst retaining view over the full water column. Image pairs were shot at a rate of 50 frames per second with a resolution of 2320 × 1726 pixels (width x height). Specifically, for water shallower than 45 cm, the resolution was 0.30 mm per pixel and for water deeper than 45 cm, the resolution was 0.35 mm per pixel.

Post-processing was conducted using Dantec's DynamicStudio 2015a to obtain water particle velocities. Best results were obtained with the

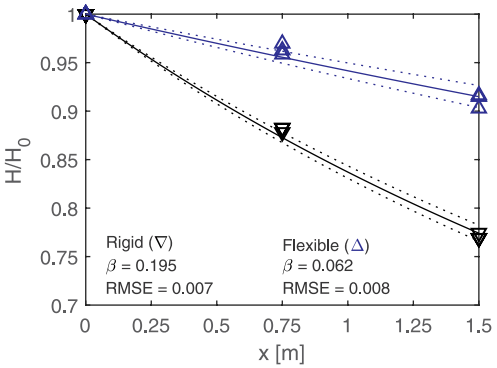

Fig. 3. Wave attenuation parameter β fitted to the wave height measurements for case R34. The triangles indicate normalized wave heights H/H_0 at each wave gauge for the three test runs. The solid lines denote the fitted attenuation function (Eq. (4)) and the dotted lines denote the 95% confidence interval. The root-mean-square error given is of H/H_0 in WG2 and WG3.

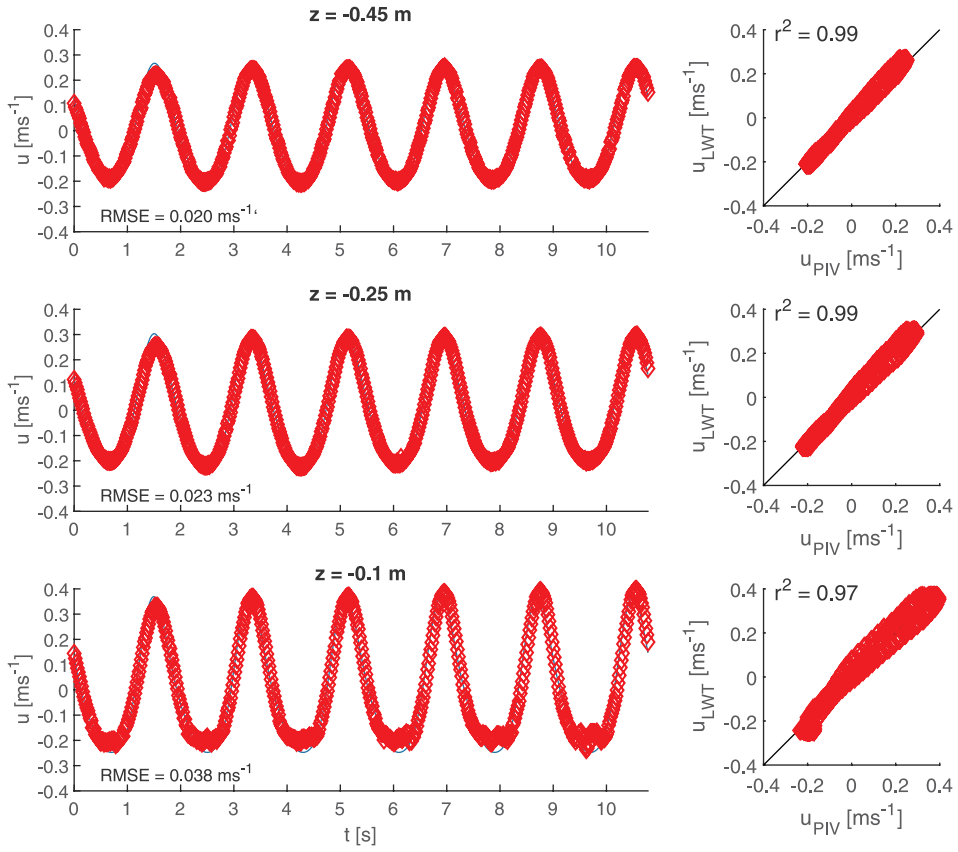

Fig. 4. Comparison of the PIV-derived particle velocity measurements for case R13 without vegetation. The blue line depicts the predicted horizontal water particle velocities based on linear wave theory using measured wave harmonics. The red diamonds depict PIV-derived water particle velocities. (For interpretation of the references to colour in this figure legend, the reader is referred to the Web version of this article.)

adaptive PIV algorithm, which calculates velocities based on cross-correlation between image pairs with interrogation areas adapted to seeding densities and flow gradients. As the observed wave motion predominantly behaved as a third-order stokes wave due to the limited water depth (Le Méhauté, 1976), the particle velocity time series at each point in the *x*-*z* plane are derived using the three primary harmonics: the natural frequency and the first and second order higher harmonics (following e.g. Luhar and Nepf, 2016). We found that higher order harmonics did not significantly improve the results. The amplitudes and phases of each harmonic are obtained using a Fast Fourier Transform analysis of the measured velocities. Importantly, the water surface elevation measurements are not used in this derivation, i.e. the resulting particle velocities are based on the PIV signal and periodicity only. The PIV-derived velocities were compared against linear wave theory for the control runs without vegetation at three points in the water column (Fig. 4). They showed excellent correlation ($r^2 \geq 0.97$) against estimates based on linear wave theory and measured wave height spectra.

The orbital velocity magnitude and net currents were obtained from the PIV-derived horizontal $u(x,z,t)$ and vertical $w(x,z,t)$ velocity signals. We define the amplitude of the magnitude of the orbital motion as

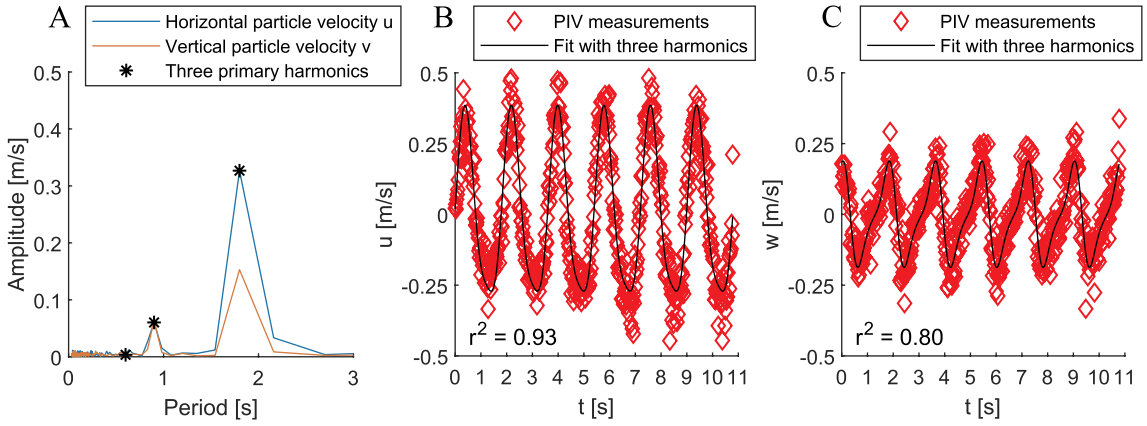

Fig. 5. Transformation of PIV output signal to a signal used in the analysis of water particle velocities for case R33 with rigid vegetation. (a) displays the Fast Fourier Transform of the horizontal (blue) and vertical (orange) particle velocities. (b) shows the quality of fit of the three harmonics (black line) with measured PIV velocities (red diamonds) for horizontal particle velocities and (c) shows this for vertical particle velocities. (For interpretation of the references to colour in this figure legend, the reader is referred to the Web version of this article.)

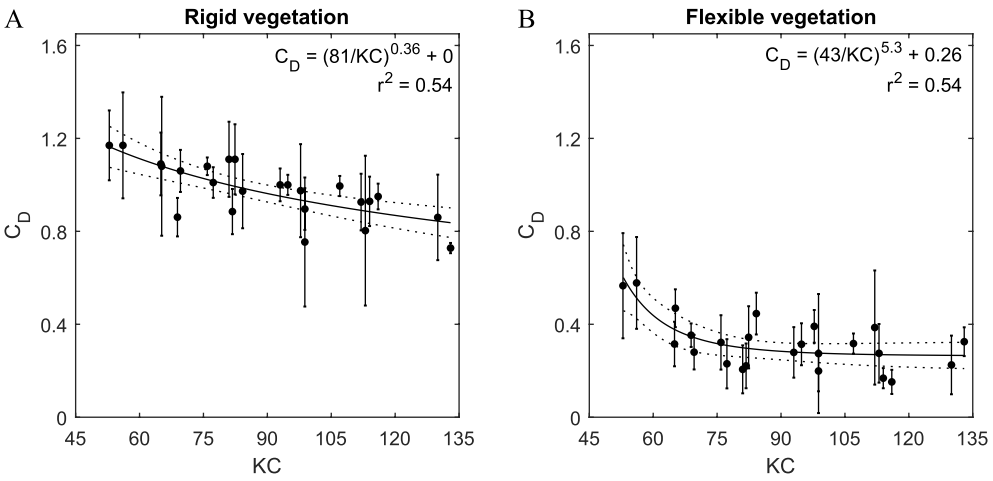

Fig. 6. Empirical relations for drag coefficient C_D as function of the Keulegan Carpenter number for (a) rigid and (b) flexible vegetation. The error bars denote the 90% confidence interval in derived C_D values and the dotted lines denotes the 95% confidence interval of the fit.

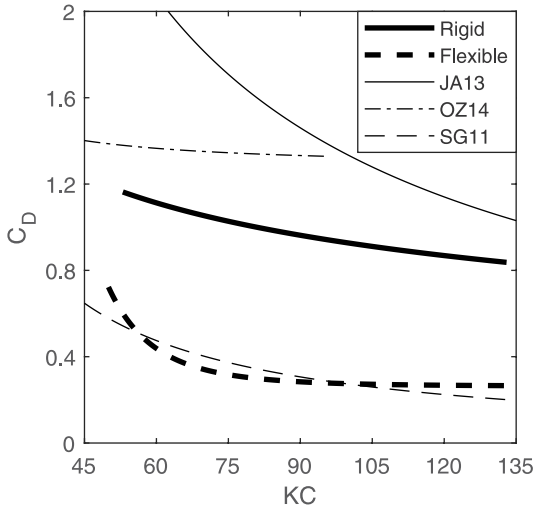

Fig. 7. Comparison of the drag coefficient relations for rigid and flexible vegetation with relations by Jadhav et al. (2013) (JA13), Ozeren et al. (2014) (OZ14), and Sánchez-González et al. (2011) (SG11).

$[u,w]_{amp}(x,z) = (\max[u,w] - \min[u,w])/2$. Hereinafter referred to as velocity amplitude, it serves as a phase-independent measure of the magnitude of the periodic orbital velocity signals. It enables comparison of velocity signals that differ in phase, which occurs over the x-z plane of a single test run and between separate test runs. Furthermore, we obtain wave-averaged net velocities $U_{net} = \frac{1}{T}\int_0^T u dt$ and $W_{net} = \frac{1}{T}\int_0^T w dt$ in horizontal and vertical direction respectively.

The main advantage of this method is that it is robust for noisy signals. This is shown for case R33 with rigid vegetation in Fig. 5, which has been identified as a case with high noise. The conditions are near emergent with the largest relative wave height. Therefore, strong wave-vegetation interaction can be expected. Yet the fit of the three primary harmonics is excellent for both horizontal ($r^2 = 0.93$) and vertical ($r^2 = 0.80$) water particle velocities.

4. Results

4.1. Drag coefficient for wave attenuation

The wave attenuation parameter β and drag coefficient C_D have been fitted for all 24 test cases on the basis of Eqs. (4) and (5). The average root-mean-square error in H/H_0 was 0.011 for rigid vegetation and 0.010 for flexible vegetation. The best fit for the drag coefficient was found to be a function of KC. Following Kobayashi et al. (1993), we used the equation

$$C_D = \left(\frac{a}{KC}\right)^b + c \tag{6}$$

to obtain a relationship between C_D and KC with $c \geq 0$. For rigid vegetation, we found

$$C_D = \left(\frac{81}{KC}\right)^{0.36} + 0 \tag{7}$$

with $r^2 = 0.54$ (Fig. 6a). Alternatively, for flexible vegetation, we obtained

$$C_D = \left(\frac{43}{KC}\right)^{5.3} + 0.26 \tag{8}$$

with $r^2 = 0.54$ (Fig. 6b). The drag coefficient of rigid vegetation is up to 70% lower for rigid vegetation than for flexible vegetation for $KC > 75$ (Fig. 7). The difference appears reduces in the range $53 < KC < 65$ but support is limited with only four conditions tested within this range.

The C_D-relations exhibit similar trends as found in earlier studies (Fig. 7). The fitted C_D of rigid vegetation is compared with fits obtained by birch dowels ($h_v = 480$mm, $b_v = 9.4$mm, $n_v = 350$ stems/m^2, EI_v not

Table 3
List of fitted coefficients in Eq. (6) across publications.

Publication	Vegetation type	a	b	c	Range	EI [Nm^2]
This study	Bamboo dowels	81	0.36	0	$53 < KC < 133$	9.0×10^{-2}
Jadhav et al. (2013)	*S. Alterniflora*	139.8	0.86	0	$25 < KC < 135$	1.5×10^{-2}
Ozeren et al. (2014)	Birch dowels	7.995	1.22	1.28	$5 < KC < 95$	Stiff
This study	Silicon rods	43	5.3	0.26	$53 < KC < 133$	1.7×10^{-5}
Sánchez-González et al. (2011)	Polyethylene blades	30.1	1.08	0	$15 < KC < 425$	4.0×10^{-7}

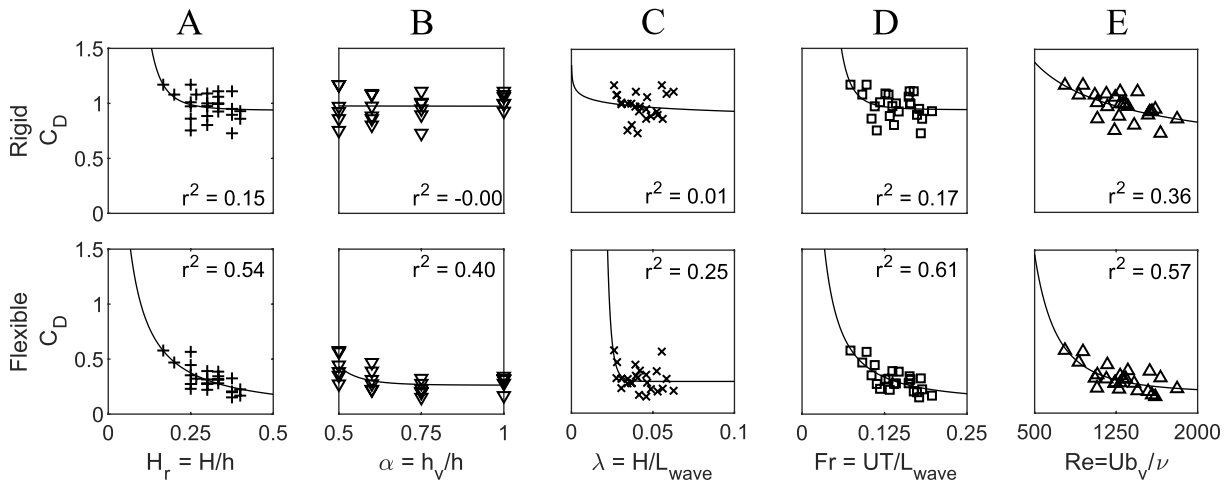

Fig. 8. Sensitivity of the drag coefficient C_D to five predictors, from left to right: (a) Relative wave height H_r, (b) submergence ratio α, (c) wave steepness λ, (d) Froude number F_r, and (e) Reynolds number Re.

reported) in Ozeren et al. (2014) and *S. Alterniflora* ($h_v = 220$ mm, $b_v = 8$mm, $n_v = 422$ stems/m^2, $EI_v = 0.015$ Nm^2) in Jadhav et al. (2013). Although *S. Alterniflora* is a natural plant, Jadhav et al. (2013) find that it can reasonably be approximated as a rigid cylinder based on their observations and its flexural rigidity value (Table 3). The C_D values found in this study are 15–50% lower than in Ozeren et al. (2014) and Jadhav et al. (2013). In case of Ozeren et al. (2014), only a small portion of their test runs was conducted within the range considered here with in the range $5 < KC < 30$ instead. In case of Jadhav et al. (2013), a possible explanation is that we observed preferential attenuation of orbital velocities within the canopy (further discussed in Section 4.3) whereas they only found preferential attenuation for a narrow frequency band based on numerical analysis. Preferential attenuation is not accounted for in Eq. (5) and will therefore lead to a reduced C_D value. Furthermore, the wave conditions and canopy density differed between this study and Jadhav et al. (2013). With respect to flexible vegetation, the fit is compared with Sánchez-González et al. (2011) who studied wave damping over polyethylene blades ($h_v = 100$ mm, $b_v = 3$mm, $n_v = 2.7\times 10^5$ stems/m^2, $EI_v = 4.0 \times 10^{-7}$ Nm^2). Fig. 7 shows that the visual agreement between the obtained fits for flexible vegetation is very good despite an increased curvature in our fit.

4.2. Sensitivity of drag coefficient to hydrodynamic parameters

To further investigate the contribution of hydrodynamic conditions to the drag coefficient, we have plotted our results against five dimensionless hydrodynamic predictors (Fig. 8): the relative wave height H_r, the submergence ratio α, wave steepness λ, Froude number F_r and vegetation Reynolds number Re. First, the relative wave height and submergence ratio address the contribution of scaled wave height and water depth. Then, wave steepness $\lambda = H/L_{wave}$ highlights the impact of wave shape, which relates to both wave period and wave height. Furthermore, $F_r = UT/L_{wave}$ is the ratio between horizontal water particle velocity with respect to wave celerity at shallow water conditions. Finally, the Reynolds number is a frequently used predictor for the drag coefficient (Anderson and Smith, 2014; Augustin et al., 2009; Hu et al., 2014; Koftis et al., 2013; Möller et al., 2014). All conditions have been fitted using a function equivalent to Eq. (6) to allow comparison with the KC number.

The results for rigid vegetation show a good fit for a relationship between C_D and Re. The r^2-coefficient for this relationship is decent with 0.36, but lower than the goodness-of-fit between C_D and KC in our experiments. Conversely, $r^2 < 0.20$ for the four other predictors. Re and KC both define their hydrodynamic length scale in terms of vegetation diameter b_v, while relative wave height, submergence ratio, wave steepness and Froude number are functions of hydrodynamic parameters only. This indicates that diameter of rigid vegetation is an important predictor for wave-vegetation interactions.

The fitted C_D for flexible vegetation correlates equally well with Re, H_r, and F_r as with the KC number. The common ground among these predictors is that higher H or U correlate with lower drag coefficients. Also, these predictors are not necessarily a function of vegetation properties such as b_v and h_v. This indicates that C_D for flexible vegetation is predominantly controlled by the hydrodynamic conditions.

4.3. Wave particle velocities

The velocity field is presented in the normalized coordinate system (x^*, z^*). The normalized horizontal axis $x^* = x/L_v$ is defined such that $x^* = 0$ represents the upstream edge and $x^* = 1$ the downstream edge of the meadow. Likewise, the normalized vertical axis $z^* = (z+h)/h_v$ is defined such that $z^* = 0$ corresponds to the flume bottom and $z^* = 1$ to the canopy of the vegetation. The PIV-window ranges from $x^* = 0.75$ to $x^* = 1.2$ for $h = 0.5$ and 0.6 m, and from $x^* = 0.8$ to $x^* = 1.15$ for $h = 0.3$ and 0.4 m.

Analysis on the velocity magnitudes focuses on the horizontal particle velocities, because they are key to the drag force (Eq. (3)), exceed the magnitude of vertical particle velocities (Fig. 5) and control the magnitude of the orbital motion (e.g. Pujol et al., 2013). Alternatively, both horizontal and vertical velocities are used for the analysis of the flow patterns. We define $U^*(x^*, z^*) = u_{amp}/u_0$ as the normalized amplitude of the horizontal velocity. $u_0(x^*, z^*)$ is the velocity profile based on linear wave theory using the three primary water surface harmonics at WG2, which is consistent with the derivation of u_{amp} (Section 3.5). It has been derived independently from the PIV-measurements and is corrected for wave attenuation. We refer to Appendix B for a detailed description. It should be noted that U^* closely resembles the attenuation parameter α_w in Lowe et al. (2005), but includes higher order harmonics and the impact of wave attenuation.

Fig. 9 displays the full normalized velocity field U^* for case R13 with rigid, flexible and no vegetation. The blank areas correspond to vegetation. The horizontal particle velocities are amplified above the rigid vegetation canopy and reduced inside (Fig. 9a). The reduction is the strongest directly below the canopy. Alternatively, the velocity field around flexible vegetation does not differ from the velocity field without vegetation (Fig. 9b and c). The gradient in the velocity field without vegetation indicates that u_0 slightly overpredicts bottom velocities ($U^* \approx 0.9$ at the bottom). Therefore, both the normalized velocity amplitude and the no vegetation cases were used as velocity references.

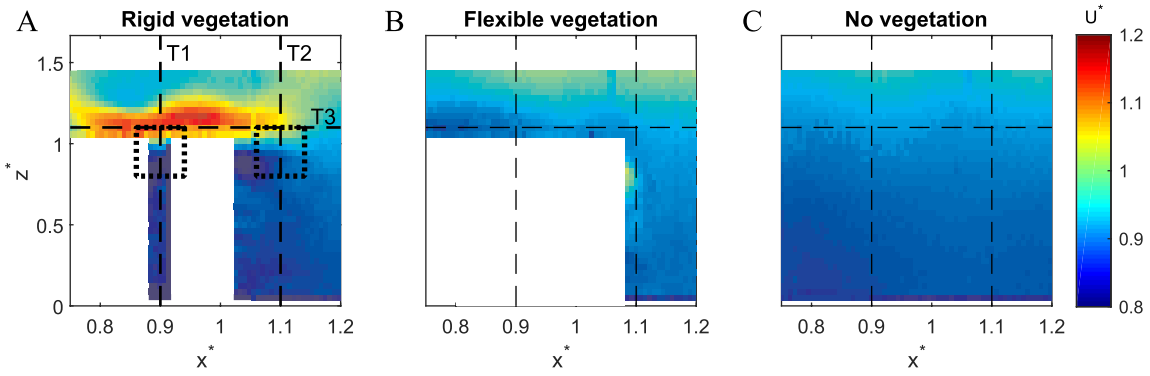

Fig. 9. Normalized horizontal particle velocity fields around (a) rigid, (b) flexible vegetation, and (c) no vegetation. All runs are conducted with condition R13. The blank areas correspond to vegetation including plant swaying. Transects T1 ($x^* = 0.9$), T2 ($x^* = 1.1$) and T3 ($z^* = 1.05$) are used in further figures. The dotted boxes denote the close-ups, which are associated with T1 and T2 respectively.

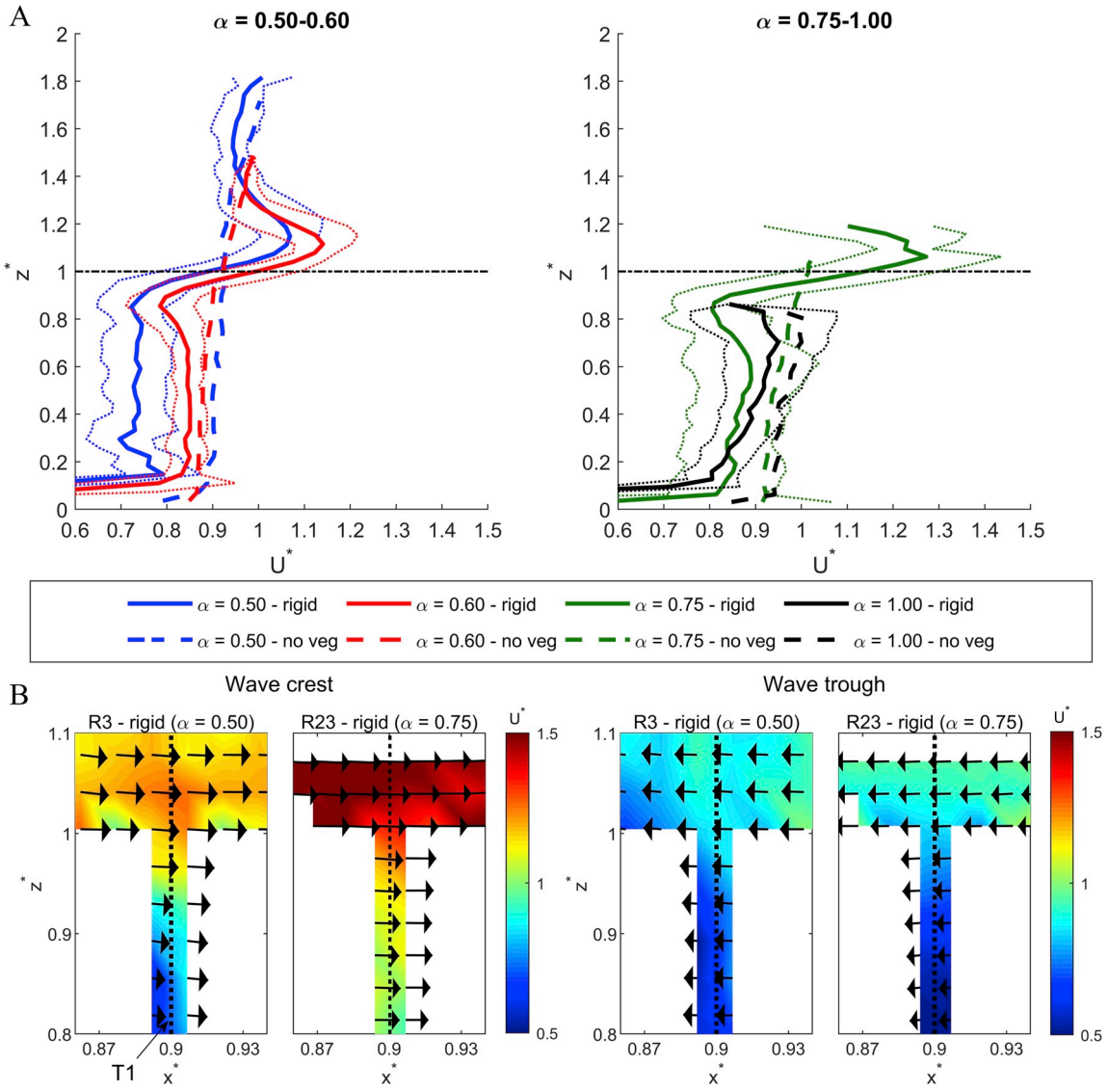

Fig. 10. Normalized particle velocity structure at transect T1, showing (a) the vertical profile of the normalized horizontal velocity magnitude at low (left) and high (right) submergence ratio, where data points are averaged over all tests with identical submergence ratio. The dotted lines denote the mean ± two standard deviations of the observations (σ). The dash-dotted line is the canopy height. (b) A close-up of the normalized velocity field around the vegetation canopy. The black vectors denote the magnitude and direction of the particle velocities. The velocities are averaged over all wave crests/troughs in a single test run. The vector density is reduced in horizontal direction by a factor of 2 for visibility. The blank areas coincide with vegetation. Finally, the dotted line represents the transect position.

The velocity fields are averaged over tests with identical submergence ratios to generalize results. They are compared along transects T1 ($x^* = 0.9$), T2 ($x^* = 1.1$) and T3 ($z^* = 1.05$), which are strategically located inside, upstream of, and over the vegetation. As swaying of flexible vegetation prevented measurements inside the canopy, T1 is evaluated for rigid and no vegetation only.

Transect T1 highlights the impact of submerged rigid vegetation ($\alpha < 1$) on the vertical velocity structure with an amplification of orbital velocities above the canopy and attenuation within (Fig. 10a). A layer with increased velocity develops directly above the canopy with its peak where $z^* \in [1.0, 1.2]$ and diminishes further above the vegetation. Conversely, the velocity amplitude is reduced inside the vegetation patch. This reduction is the strongest in the layer directly below the canopy where $z^* \in [0.8, 1.0]$ and decreases near the bottom. However, an exception is the deep submerged case $\alpha = 0.50$ for which velocities are diminished strongly over the full vegetation column. The impact of emergent rigid vegetation is lower than submerged vegetation. The normalized velocity amplitude displays a gradient over the vegetation column, with higher velocities near the canopy and lower velocities near the bottom. This may be related to wave crests that still elevate above the canopy for given conditions.

The plant submergence ratio α appears to be a key parameter in quantifying the velocity structure, because it controls whether an amplified layer develops and the magnitude of the velocities therein. The velocity amplification increases with the submergence ratio with maximum amplification observed at $\alpha = 0.75$ with $U^* = 1.25$. Furthermore, the standard deviation of the normalized horizontal velocity structure is low ($\sigma = 0.02 - 0.08$) at any given water depth despite variations in wave period and height. This supports the notion of α as a key parameter.

Finally, normalized velocity vectors around the canopy show the velocity gradient between the amplified and the attenuated water layers (Fig. 10b). The velocities are amplified above the vegetation under a wave crest and attenuated below the canopy during the wave trough. The velocities above the canopy at wave trough are as expected from linear wave theory. The stronger amplification of case R23 under wave crests agrees with the positive correlation of submergence ratio on amplification.

Alternatively, the impact of vegetation at cross-section T2 is small for both rigid and flexible vegetation (Fig. 11). This location was selected as it is just outside the range of vegetation swaying, allowing for an inclusion of flexible vegetation in the analysis. It turns out that the normalized orbital velocity structure is constant over the water depth for all cases. At the same time, U^* for both rigid and flexible vegetation is

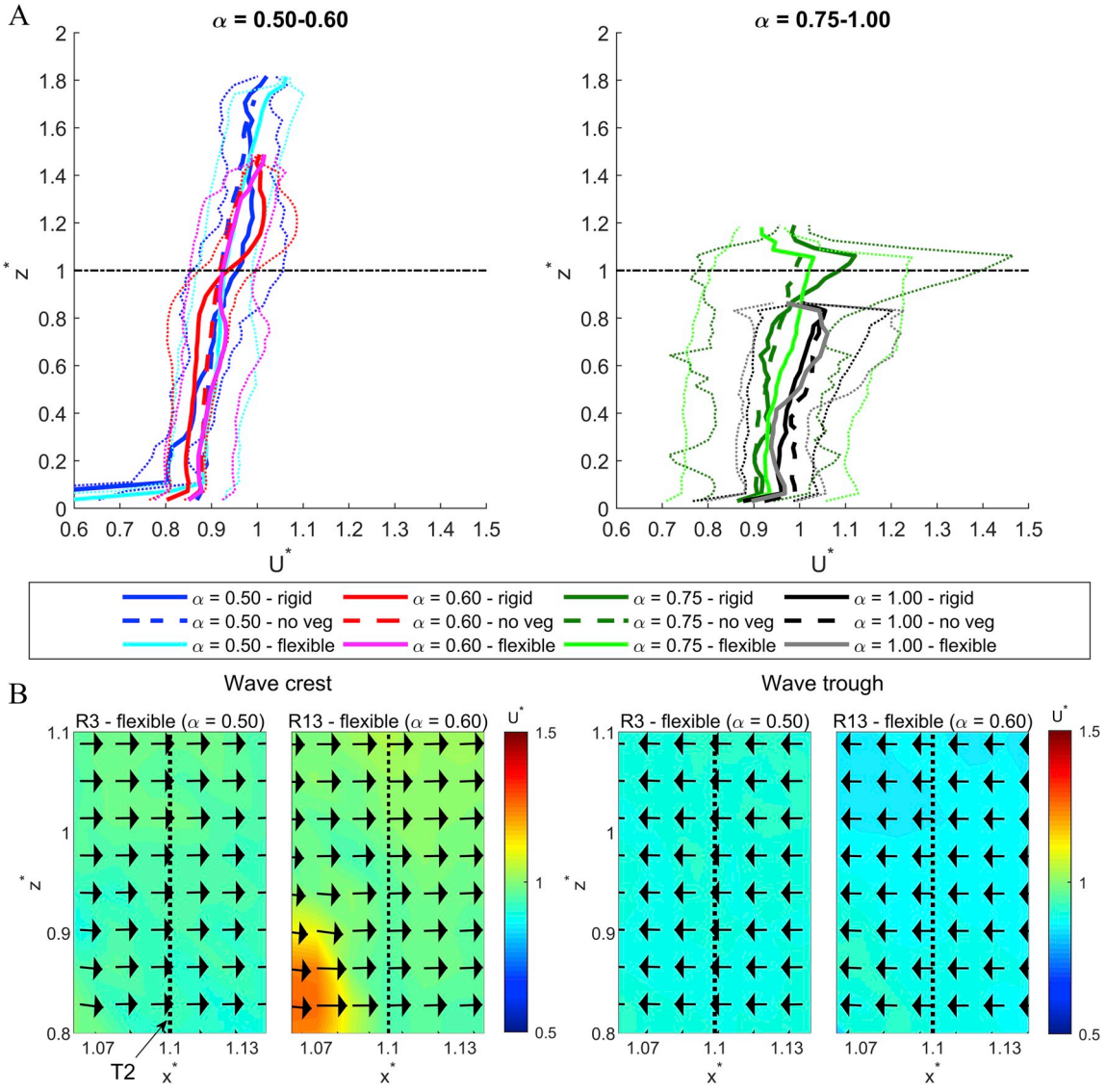

Fig. 11. Normalized particle velocity structure at transect T2. See Fig. 10 for a full description.

close to the respective reference case without vegetation for all water depths. The only exception is an amplification by rigid vegetation at $\alpha = 0.75$, when $U^* = 1.12$ at $z^* = 1.05$, but this is much smaller than at transect T1 and coincides with the highest variability in the observations.

Rigid vegetation appears to be key for the development of a water layer with amplified orbital velocities directly above the canopy. Fig. 12 shows U^* at $z^* = 1.05$ as a function of x^*. This elevation matches the peak net velocities in Fig. 10. The data gaps coincide with the position of WG3. The cases with flexible vegetation and without vegetation all display a constant normalized velocity amplitude of $U^* =$ 0.90–0.93. Conversely, all three cases with submerged rigid vegetation feature an amplified layer with $U^* \approx 1.05$ for $\alpha = 0.50$, $U^* \approx 1.13$ for $\alpha = 0.60$ and $U^* \approx 1.23$ for $\alpha = 0.75$. Furthermore, the amplification is relatively constant over the vegetation length within the PIV-window, which suggests that the velocity field is unaffected by the gap at $x^* = 0.9$. The velocity amplification reduces linearly downstream of the vegetation and returns to its normal level at $x^* = 1.15$.

Furthermore, we find that rigid vegetation can induce two types of flow circulation depending on the submergence ratio. A net downstream current develops around $z^* = 1$ for both submerged and emergent vegetation at transect T1 (Fig. 13a). This is compensated by an upstream current high above the canopy for deep submerged vegetation ($\alpha \leq 0.60$) or within the vegetation for emergent and near-emergent vegetation ($\alpha \geq 0.75$). The former results in a counter-clockwise circulation above the vegetation and the latter in a clockwise circulation through the vegetation.

The net currents at transect T2 support the presence of flow rotations over and through the vegetation. The circulations identified over and through rigid vegetation can still be identified, but with reduced net downstream velocities of up to 0.015 m/s instead of 0.040 m/s (Fig. 13b). The decrease in net horizontal velocities at transect T2 for rigid vegetation comes with an increase of net vertical velocities consistent with the rotational motion (Fig. 13c). A net upward velocity develops for deeper submerged rigid vegetation cases, which is associated with counter-clockwise motion. Alternatively, net downward currents develop below the canopy for the near-emergent case, which are consistent with clockwise rotation through the vegetation. The circulation for emergent rigid vegetation can no longer be identified, which may indicate that the rotation develops on a shorter scale.

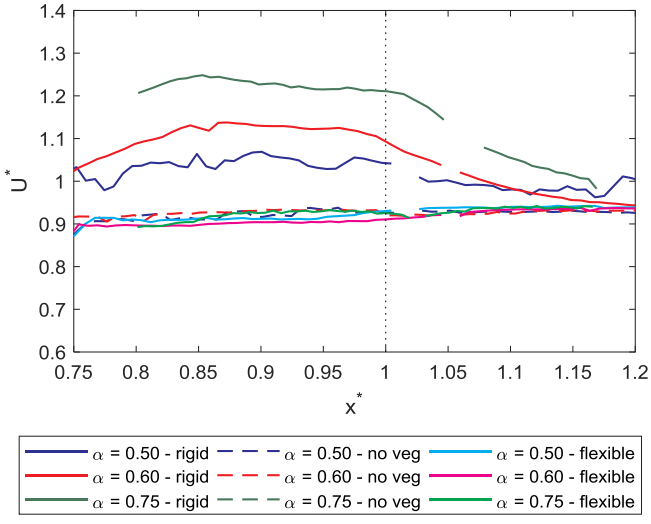

Fig. 12. Normalized velocity U* as function of along patch coordinate $x^* = x/L_v$ at transect T3 ($z^* = 1.05$). Results are averaged over all runs with equal submergence ratio and vegetation type. The dotted line represents the downstream edge of the vegetation. The data gaps coincide with interference from WG3.

Interestingly, a 0.01 m/s net downstream stream current is also identified for flexible vegetation at $\alpha = 0.60$, but not at other submergence ratios (Fig. 13d). The corresponding upstream currents are equally distributed over and through the vegetation. It is unclear whether this is a local circulation induced by the edge of the swaying motion or a larger circulation around the vegetation patch. Especially, because it is not identified for deeper submergence and the net vertical velocities (Fig. 13e) do not provide further support. Currents at other submergence ratios do not exceed 0.005 m/s.

5. Discussion

5.1. Impact of plant flexibility on wave attenuation

Stem flexural rigidity appears to be a key parameter for determining the drag coefficient for wave attenuation. Our results show that the drag coefficient of flexible vegetation is up to 70% lower than rigid vegetation under identical hydrodynamic conditions (Fig. 7). This decrease is of the same order as has been estimated previously. Mullarney and Henderson (2010) and Maza et al. (2013) studied the impact of plant swaying on drag force using numerical models. They found 70% and 50% reductions in drag coefficients respectively. Alternatively, Riffe et al. (2011) find 50% reduction in drag force for flexible vegetation in a field study. The magnitudes of the reductions in wave damping by flexible vegetation are in the same order of magnitude despite differences in plant morphology (cylindrical versus blades), wave conditions, and flexural rigidity of the flexible vegetation.

The reduced wave damping capacity of flexible vegetation has been attributed to vegetation swaying. The physical explanation is two-fold. First, swaying of the vegetation reduces the frontal area of the vegetation. This reduces the total work that can be exercised by the drag force and, consequently, directly reduces the energy lost in a wave travelling over vegetation (Dalrymple et al., 1984). Secondly, the relative velocity between water and vegetation reduces when vegetation sways with the flow (Méndez et al., 1999). These effects are not accounted for in Eq. (5) and will thus lead to a lower calibrated drag coefficient.

The negative impact of plant swaying on wave attenuation is supported by our experimental results and literature. First, we found that drag coefficient for flexible vegetation correlated equally well to predictors that related to wave conditions only, whereas the drag coefficient for rigid vegetation only related well to predictors that did include stem diameter (Fig. 8). This indicates that flexible vegetation follows flow and rigid vegetation controls flow. Furthermore, Möller et al. (2014) found low drag coefficients for plants with low flexural rigidities. Also, they were observed to sway significantly (Rupprecht et al., 2017). In a separate study on a limited number of plant mimics, Paul et al. (2016) also identified the reduction in stem frontal area via stem bending as a key parameter in the prediction of the drag coefficient.

5.2. Wave-induced circulation

Wave-averaged velocity fields from our experiment show that the mean currents drive a circulation over or through rigid vegetation, depending on the submergence ratio (Fig. 14). Like prior studies (Abdolahpour et al., 2017; Pujol et al., 2013), we find a mean current in the direction of wave propagation around the canopy. This net downstream current has been associated with boundary layer streaming, which follows from the shear stresses at the top of the vegetation (Luhar et al., 2010; Pujol et al., 2013). As the flume is a closed system, a mean current in the direction of wave propagation must be compensated for by a return flow. Under sufficiently submerged conditions ($\alpha \leq 0.60$), the return flow occurs in the region between the top of the vegetation canopy and free surface. However, as a vegetation-free region is not available under shallow conditions ($\alpha \geq 0.75$), the return flow passes through vegetation itself. This results in an anti-clockwise circulation, when current returns above the canopy (Fig. 14, top row) or a clockwise

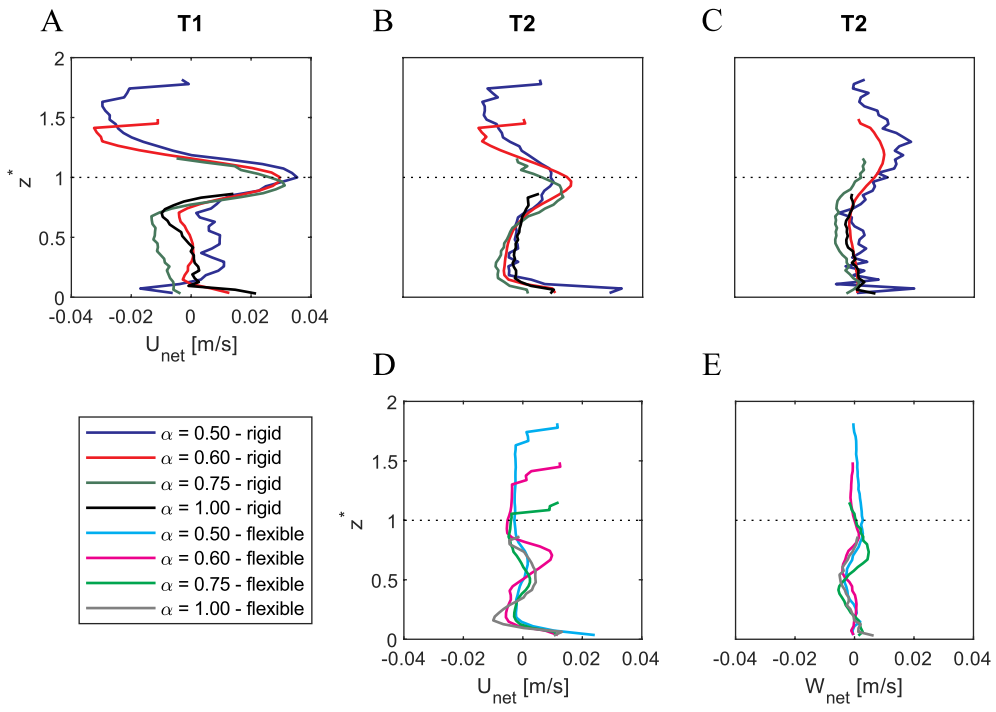

Fig. 13. Vertical profile of wave-averaged net velocities: (a) net horizontal velocities at T1; (b) & (d) net horizontal velocities at T1; (c) & (e) net vertical velocities at T2. The top row features rigid vegetation and the bottom row flexible vegetation.

circulation through the vegetation, when the current returns inside the canopy (Fig. 14, middle row).

Our velocity fields extend the framework for velocity structures as proposed by Pujol et al. (2013). We compare results for submerged ($\alpha = 0.50$, Fig. 14: top row) and emergent ($\alpha = 1.0$, Fig. 14: middle row) rigid vegetation and submerged flexible vegetation ($\alpha = 0.50$, Fig. 14: bottom row). The circulations over and through rigid vegetation in our study fit their vertical velocity structure inside the meadow. Both studies show a mean current in the direction of wave propagation through the canopy and a return flow that depends on submergence ratio. Results also agree that flexible vegetation does not impact the flow field.

The circulation through a flexible meadow, as described by Luhar et al. (2010) could not be reproduced. The submergence ratio $\alpha = 0.50$, which was used in Luhar et al. (2010), did not lead to the generation of mean currents (Fig. 14, bottom row). We find a weak mean current in the direction of wave propagation when $\alpha = 0.60$, but its magnitude and position do not agree with Luhar et al. (2010). Forcing with a smaller wave amplitude, they find net velocities up to 0.073 m/s, which even exceed net current velocities induced by rigid vegetation in our study by a factor of two. Furthermore, the position of the peak velocity is located at $z^* = 0.35$ in Luhar et al. (2010) compared to $z^* = 0.70$ in our study. Disagreements may be related to the difference in the geometry of vegetation used in the two studies. Luhar et al. (2010) used blades instead of stems where six blades were attached to a single point in the flume bottom. Therefore, the stem spacing can be wider near the bottom than in the canopy, which may promote convergence of the current in this area. Also, the higher frontal area for blades (up to $\lambda_f = 4.2$) as opposed to cylinders ($\lambda_f = 1.7$) may have contributed to the different observations (Abdolahpour et al., 2017).

Differences between rigid and flexible vegetation are consistent with Abdolahpour et al. (2017). They developed an empirical relation for the magnitude of wave-driven currents as function of the vertical particle excursion, plant dimensions and drag coefficient. Specifically, the drag coefficient correlates positively to the magnitude of the wave-driven currents. Our results show that rigid vegetation has a higher drag coefficient than flexible vegetation and will therefore develop significant net currents at lower vegetation densities and wave heights.

The presence of flow circulations around vegetation implies that the wave-current field is not uniform and irrotational. The vegetation patch acts, from a hydrodynamic perspective, as a source of vorticity. This may affect wave shape and, thereby, Equations (1)–(5) which assume a sinusoidal wave shape (Dalrymple et al., 1984). A detailed analysis of the wave shape and its implications is beyond the scope of this study, but it may have affected the drag coefficient which acts as calibration parameter.

5.3. Orbital velocity structure

The wave orbital velocity structure under rigid vegetation is characterized by a layer of amplified orbital velocity directly above the canopy and a layer of reduced orbital velocity directly below it (Fig. 10). Orbital velocities far above or far below the canopy appear to be unaffected. Conversely, flexible vegetation appears not to impact the velocity structure. This section will therefore focus on rigid vegetation only.

Our findings agree with Koftis et al. (2013), who found that for a set of point measurements, maximum orbital velocities in the water column were attained directly above the vegetation. However, others found that the velocities within the meadow were uniformly attenuated and did not observe an amplified layer above the vegetation (Lowe et al., 2005; Luhar et al., 2010; Pujol et al., 2013).

The lack of strong attenuation of orbital velocities inside the vegetation patch, appears to be related to the layout of the vegetation canopy. Lowe et al. (2005) showed that velocity attenuation is a function of the ratio of wave excursion to stem spacing ($U/\omega S_v$) and the ratio of stem spacing to stem diameter (S_v/b_v). In this study, $U/\omega S_v = O(10^{-2})$ and $S_v/b_v = 6$ relate to inertia dominated flow with large stem spacing. Both contribute to low velocity attenuation within the canopy. For example, Lowe et al. (2005) show that attenuation is absent for inertia dominated flow with $S_v/b_v = 7.8$.

We propose that water layers with the amplified/diminished velocities above and below the canopy, which were observed in detail for the first time in this study, follow from an unsteady wave-induced net current (Section 5.2). This is shown by analysing horizontal particle

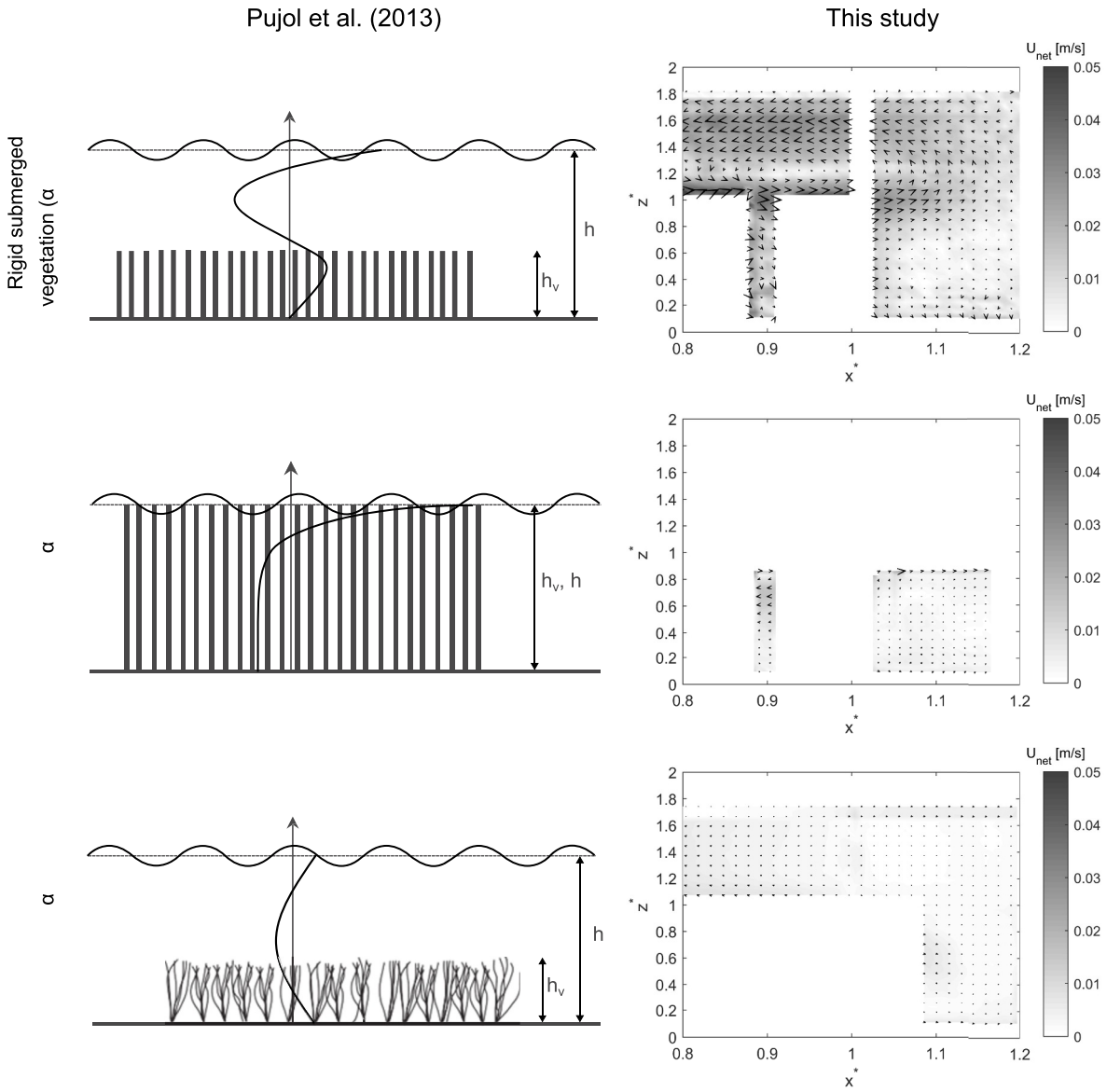

Fig. 14. Wave-averaged mean velocity fields as proposed Pujol et al. (2013; left column) and found in this study (right column) under equal submergence ratios: submerged rigid vegetation ($\alpha = 0.50$, top row), emergent rigid vegetation ($\alpha = 1.0$, middle row) and submerged flexible vegetation ($\alpha = 0.50$, bottom row). The gap in the top row coincides with WG3. Further blank areas correspond to vegetation, including swaying for (c).

velocity differences between run R13 with rigid vegetation and without vegetation for five wave cycles (Fig. 15). The net current that results from the wave-vegetation interaction can be clearly identified by the red colour around the canopy (black dashed line). This current flows above and below the canopy over a wave cycle. Specifically, the current acts above the canopy when a wave crest passes and below when a trough passes. Thus, it appears at a constant relative depth such that the mean depth is at the vegetation canopy.

As the mean current is in the direction of wave propagation, it is aligned with the horizontal orbital velocities at wave crests, leading to velocity amplification directly above the canopy. Equally, it opposes the horizontal orbital velocities during wave troughs, leading to attenuation directly below the canopy. Both effects are confirmed by temporal analysis of selected points in Fig. 15b&c. Other velocity differences can be attributed to slight differences in wave shape as a result of rigid vegetation.

5.4. Length of the vegetation field

The length of the vegetation field used in this study is 1.5 m. Although longer canopies may provide additional data to confirm observed trends, we believe that the length of the experimental canopy is sufficient for the wave dynamics to adjust to the presence of vegetation. The adjustment length is controlled by the canopy drag length (Coceal and Belcher, 2004; Lowe et al., 2005), according to

$$L_D = \frac{2h_v(1-\lambda_p)}{C_{SD}\lambda_f} \tag{9}$$

where $\lambda_p = \pi b_v^2 n_v/4$ is the vegetated area per unit ground area and C_{SD} is the sectional drag coefficient. C_{SD} differs from C_D as it relates to the in-canopy flow velocity rather than the ambient flow velocity and does not include plant swaying through calibration (Lowe et al., 2005). An estimate of C_{SD} is made by correcting the fitted drag coefficient of rigid vegetation (Eq. (7)) for in-canopy velocity attenuation. The observed attenuation is around 20% (Fig. 10a) and $C_D \propto U^{-3}$ when derived through

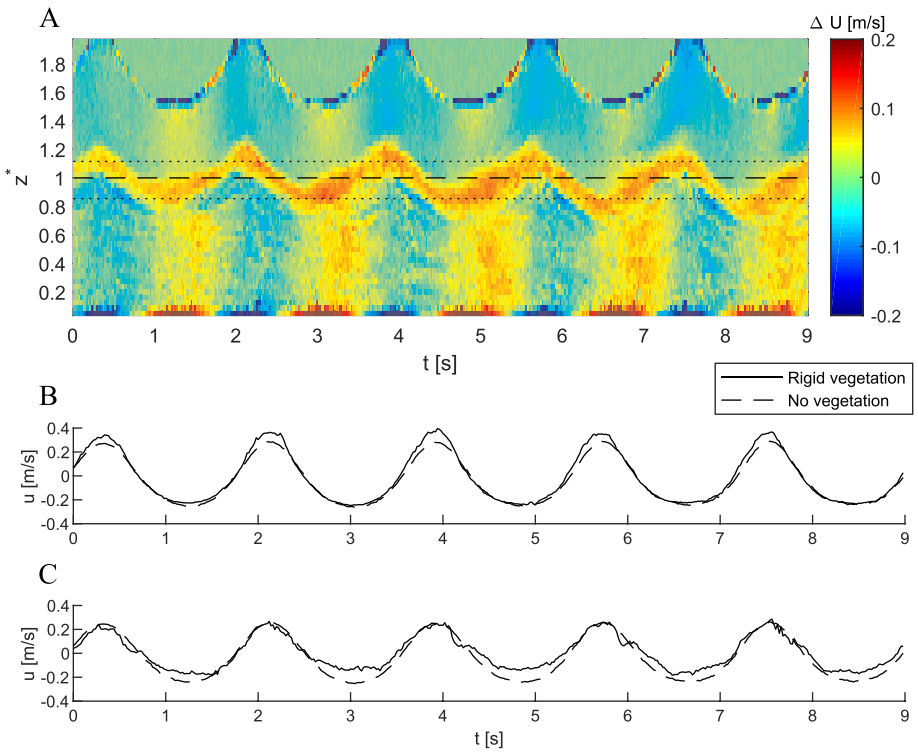

Fig. 15. Difference in horizontal particle velocities between rigid vegetation and no vegetation under equal wave conditions (R13). Results are presented over five wave cycles ($T = 1.8$ s). Top plot (a) displays the temporal variation along cross-section T1. Herein, the dashed line depicts the canopy, the top dotted line corresponds to the location of plot (b) and the bottom dotted line to plot (c). Middle plot (b) shows observed horizontal particle velocities at $z^* = 1.1$ with rigid vegetation and without vegetation. Likewise, bottom plot (c) presents observed horizontal particle velocities at $z^* = 0.85$.

wave height measurements (Eqs. (1), (3) and (5)). Therefore, we estimate

$$C_{SD} = \left(\frac{520}{KC}\right)^{0.36}. \tag{10}$$

At $KC = 133$ which is the conservative limit of our range, $C_{SD} = 1.63$. Furthermore, $\lambda_f = 1.67$ and $\lambda_p = 0.022$. We find that $L_D \approx 0.22$m and $L_v/L_D = 6.9$ (in-canopy velocity measurements at $6.2L_D$). Lowe et al. (2005) find that the adjustment length is $3L_D$-$5L_D$ which is satisfied by our experimental conditions. Our experimental results the along horizontal transect T3 (Fig. 12) also suggest the velocity structure has adjusted to the presence of vegetation as the velocity amplitude remains constant over the back section of the vegetation which has been the focus of our measurements. Finally, we note that the observed wave damping over the vegetation field is significant as it ranges between 2% and 25% depending on vegetation and wave conditions.

5.5. Implications for nature-based coastal defences

Most natural salt marsh vegetation exhibits a mix of rigid shrubs and flexible grasses. These mixed marshes are not only beneficial for biodiversity, but combined rigid and flexible vegetation is complementary to coastal protection. While both attenuate wave energy, the damping capacity of rigid vegetation exceeds that of flexible vegetation. Foreshores with rigid vegetation can be up to 70% thinner than foreshores with flexible vegetation to provide the same level of protection. It is expected that the level of protection that semi-flexible vegetation provides will be between the limits of rigid and flexible vegetation. Furthermore, the wave-induced currents in rigid vegetation patches can promote sediment transport to the higher marshes, potentially increasing marsh accretion. This may enable marshes to increase elevation to combat potential impacts of sea level rise and can act as a buffer against extreme events. Alternatively, swaying of flexible plants can prevent stem breaking (Rupprecht et al., 2017; Vuik et al., 2018). Therefore, flexible species can be expected to remain effective during higher wave energy conditions.

However, the differences in plant flexibility have to be considered when modelling the impact of mixed vegetation salt marshes on hydrodynamics and wave height. Much research effort has been invested in finding single relations to predict a drag coefficient for salt marshes (e.g. Losada et al., 2016; Möller et al., 2014). While these have led to useful relationships and have proven the capacity to model wave attenuation, the relations may only be applicable for a specific set of species, or rather a specific combination of plant flexibilities used in such experiment.

In contrast, this study has identified different wave-vegetation interactions between the rigid and flexible limits and provides drag coefficients associated with these limits. Although the mimics have been based on the South Wales salt marshes, the results show wave attenuation to be a function of plant flexibility. The range of flexural rigidities in South Wales is wide and also covers, for instance, the species in US salt marshes (Chatagnier, 2012; Feagin et al., 2011). Therefore, our results have a wider application.

6. Conclusions

A laboratory study under controlled conditions using artificial rigid and flexible vegetation has provided us with the opportunity to study the impact of plant flexibility on the drag coefficient and the velocity structure. For the first time, we test mimics that differ in flexural rigidity only under conditions that have been directly derived from the field. We have selected rigid and flexible vegetation mimics that represent a wide range of plant flexibilities found in typical South Wales salt marshes. Drag coefficients were derived from measured wave attenuation and, as a further novelty, we have measured the velocity field in and around the vegetation using PIV.

Our results show that both rigid and flexible vegetation damp waves, but rigid vegetation provides superior damping. This is expressed via a drag coefficient; i.e. a higher drag coefficient means stronger damping. We find that the drag coefficient for flexible vegetation is up to 70% lower than for rigid vegetation. Plant swaying of flexible vegetation reduces the plant frontal area and the relative velocity difference between plants and water. Both have a negative effect on the drag forces and associated energy losses. As a result, swaying flexible plants will

damp waves less than rigid plants that do not sway.

Furthermore, we find that rigid vegetation alters the velocity structure, while flexible vegetation does not. Specifically, the interaction between waves and rigid vegetation induces a current in the direction of wave propagation through the top of the vegetation. This current propagates above and below the canopy in phase with the water surface. For submerged vegetation, this results in amplified horizontal particle velocities above the vegetation canopy and reduced velocities within the vegetation. The magnitude of the current and the amplification depend on submergence ratio. A stronger current and amplification develop for higher submergence ratios. Finally, a return current develops high in the water column when the vegetation is sufficiently submerged or, otherwise, through the meadow.

Based on these outcomes, it can be concluded that different salt marshes may provide different levels of protection against wave action, depending on the flexibility of established species. A single drag coefficient for salt marshes may not exist. Plant flexibility appears to be a key control parameter when defining a drag coefficient for a given salt marsh. This study has set out the limits and impacts of the latter, but additional research is required to further quantify the impact of plant flexibility and associated swaying to predict drag coefficients for a wide range of habitats. The next step would be to search for a governing relation between drag coefficient and plant flexibility, which will be addressed in a follow-on study.

Declaration of competing interest

The authors declare that they have no known competing financial interests or personal relationships that could have appeared to influence the work reported in this paper.

CRediT authorship contribution statement

Thomas J. van Veelen: Conceptualization, Methodology, Investigation, Formal analysis, Writing - original draft. **Tom P. Fairchild:** Investigation, Resources, Writing - review & editing. **Dominic E. Reeve:** Resources, Writing - review & editing, Supervision. **Harshinie Karunarathna:** Conceptualization, Methodology, Writing - review & editing, Supervision.

Acknowledgements

We thank Dr. J.M. Horrillo-Caraballo, T.S. Orimoloye and Dr. A.A. Zuhaira, Swansea University, for their invaluable assistance during the experiments. We also thank Dr. W.G. Bennett for his support in the field work and Dr. S. Alton for providing equipment and assistance in the stem bending tests. Finally, we thank one anonymous reviewer whose comments have greatly improved the quality of this manuscript. TvV acknowledges support for his PhD by Swansea University. This research formed part of the Valuing Nature Programme (valuing-nature.net) which is funded by the Natural Environment Research Council, the Economic and Social Research Council, the Biotechnology and Biological Sciences Research Council, the Arts and Humanities Research Council and the Department of the Environment, Food and Rural Affairs. This research was supported by the UK Research Councils under Natural Environment Research Council award NE/N013573/1, Title CoastWEB: Valuing the contribution which COASTal habitats make to human health and WEllBeing, with a focus on the alleviation of natural hazards.

Appendix A. Data collection in South Wales estuaries

A.1 Plant data

Salt marshes in South Wales are generally sheltered and exhibit a mix of shrubby and grassy species, among which *Atriplex Portulacoides*, *Spartina Anglica*, *Festuca Rubra*, *Puccinellia Maritima*, and *Aster Tripolium* are most common. Data for these species has been obtained from field campaigns in the Taf (August 2017) and Neath (April 2018) estuaries. These two estuaries are typical of small, macro-tidal estuaries found in Wales, UK which contain a substantial expanse of salt marshes. Plant density was measured in the field and at least 9 samples of each specie were brought to the lab for further analysis from both sites (Table A1).

The samples were pressed against a lightbox and photographed to obtain plant morphology, which was used to derive stem height, stem diameter and the number of stems per plant. The mean values of stem height ranged from 231 mm (*F. Rubra*) to 590 mm (*S. Anglica*) and stem-averaged diameters from 0.74 mm (*F. Rubra*) to 5.50 mm (*A. Tripolium*). Furthermore, the number of stems per plant was multiplied by plant density to obtain stem density values. These ranged from 214 stems/m^2 (*A. Tripolium*) to 36000 stems/m^2 (*F. Rubra*). The corresponding frontal area λ_f varied between 0.57 m^2 (*A. Tripolium*) and 6.08 m^2 (*F. Rubra*) per m^2 ground area.

Furthermore, plant flexural rigidities were obtained via bending tests, following Miler et al. (2012) and Paul et al. (2014). *A. Portulacoides*, *P. Maritima*, and *F. Rubra* were subjected to a three-point bending test, while a four-point bending test was applied to *S. Anglica* and *A. Tripolium* to avoid stem denting. However, only 4 samples of *S. Anglica* and *A. Tripolium* were viable. A mixture of top, middle and bottom stem sections were tested for all species. Ultimately, Young's moduli E ranged from 139 MPa (*S. Anglica*) to 2343 MPa (*F. Rubra*) and corresponding flexural rigidities EI ranged from 2.6×10^{-2} Nm^2 (*A. Tripolium*) to 1.9×10^{-5} Nm^2 (*P. Maritima*).

Table A.1
List of measured plant data on South Wales salt marshes. The number of samples n is given separately for geometrical and mechanical tests. Standard deviation σ is given for key parameter E.

Specie	h_v[mm]	b_v[mm]	n_v[m^{-2}]	λ_f [-]	n [-]	E[MPa]	σ[MPa]	EI[Nm^2]	n [-]
A. Portulacoides	334	2.58	2275	1.96	72	745	355	1.6×10^{-3}	10
S. Anglica	590	3.33	720	1.42	72	139	71	8.4×10^{-4}	4
P. Maritima	335	0.85	3444	0.98	27	757	382	1.9×10^{-5}	15
F. Rubra	231	0.74	36000	6.08	9	2343	2006	3.4×10^{-5}	11
A. Tripolium	487	5.50	214	0.57	24	572	469	2.6×10^{-2}	4

A.2 Wave properties

Wave conditions were determined by numerical modelling of wave penetration into a sheltered macro-tidal estuary, which is typical of South

Wales (Benett et al., pers. comm.). Results for moderate storm conditions are used, because these occur more frequently and have a larger impact on salt marsh deterioration (Leonardi et al., 2016). Typical wave parameters for these conditions are the significant wave height $H_s = 0.1 - 0.2$ m, peak period $T_p = 2$ s and water depth $h = 0 - 0.6$ m.

Appendix B. Linear velocity estimation

Linear velocity amplitude u_0 is derived from linear wave theory, using the water surface elevation harmonics from WG2 at the centre of the vegetation patch. The three primary water surface harmonics are used, which is consistent with the PIV-derived velocity signals. Following linear wave theory, the orbital velocities can be expressed as

$$u_{00}(z,t) = \sum_{n=0}^{2}\left(\frac{\eta_{amp,n} g k_n}{\omega_n}\frac{\cosh[k_n(h+z)]}{\cosh(k_n h)}\cos(\omega_n t + \varphi_n)\right) \tag{B.1}$$

where subscript n denotes the order of the harmonic of each parameter. $n = 0$ denotes the natural frequency and $n = 1, 2$ refers to the first and second order harmonics respectively. u_{00} is the reference horizontal velocity profile at WG2. Furthermore, η_{amp} is the amplitude of the water surface motion, $\omega = 2\pi/T$ is the wave frequency and φ is the wave phase. Like the PIV velocity signals, the velocity amplitude can now be obtained via the maximum and minimum of the time series at each point in the water column, expressed as $u_{00,amp}(z) = [\max(u_{00}) - \min(u_{00})]/2$.

However, the WG2 is located at the centre of the vegetation patch and wave attenuation continues downstream. Therefore, the reference velocities are corrected over along-patch coordinate x (we refer to Section 2 for details), according to

$$u_0(x,z) = \frac{u_{00,amp}}{1 + \beta[\min(x, L_v) - x_{WG2}]} \tag{B.2}$$

Herein, u_0 is a spatially varying reference velocities corrected for wave attenuation. We reiterate that $x = 0$ depicts the front edge of the vegetation. Furthermore, $x_{WG2} = 0.75$ m is the position of WG2 and $x = L_v$ is the downstream edge of the vegetation, beyond which waves do not further attenuate.

We now define non-dimensional velocity $U^* = u_{amp}/u_0$. It closely resembles attenuation parameter α_w in Lowe et al. (2005). However, U^* also includes higher order harmonics and the impact of wave attenuation.

Appendix C. Supplementary data

Supplementary data to this article can be found online at https://doi.org/10.1016/j.coastaleng.2020.103648.

References

Abdolahpour, M., Hambleton, M., Ghisalberti, M., 2017. The wave-driven current in coastal canopies. J. Geophys. Res. Oceans 122, 3660–3674. https://doi.org/10.1002/2016JC012446.

Anderson, M.E., Smith, J.M., 2014. Wave attenuation by flexible, idealized salt marsh vegetation. Coast. Eng. 83, 82–92. https://doi.org/10.1016/j.coastaleng.2013.10.004.

Augustin, L.N., Irish, J.L., Lynett, P., 2009. Laboratory and numerical studies of wave damping by emergent and near-emergent wetland vegetation. Coast. Eng. 56, 332–340. https://doi.org/10.1016/j.coastaleng.2008.09.004.

Bouma, T.J., van Belzen, J., Balke, T., Zhu, Z., Airoldi, L., Blight, A.J., Davies, A.J., Galvan, C., Hawkins, S.J., Hoggart, S.P.G., Lara, J.L., Losada, I.J., Maza, M., Ondiviela, B., Skov, M.W., Strain, E.M., Thompson, R.C., Yang, S., Zanuttigh, B., Zhang, L., Herman, P.M.J., 2014. Identifying knowledge gaps hampering application of intertidal habitats in coastal protection: opportunities & steps to take. Coast. Eng. 87, 147–157. https://doi.org/10.1016/j.coastaleng.2013.11.014.

Bullock, G.N., Crawford, A.R., Hewson, P.J., Walkden, M.J.A., Bird, P.A.D., 2001. The influence of air and scale on wave impact pressures. Coast. Eng. 42, 291–312. https://doi.org/10.1016/S0378-3839(00)00065-X.

Camfield, F.E., 1983. Wind-wave growth with high friction. J. Waterw. Port, Coast. Ocean Eng. 109, 115–117. https://doi.org/10.1061/(ASCE)0733-950X(1983)109:1(115).

Chatagnier, J., 2012. The Biomechanics of Salt Marsh Vegetation Applied to Wave and Surge Attenuation. LSU Masters Theses.

Chen, H., Ni, Y., Li, Y., Liu, F., Ou, S., Su, M., Peng, Y., Hu, Z., Uijttewaal, W., Suzuki, T., 2018. Deriving vegetation drag coefficients in combined wave-current flows by calibration and direct measurement methods. Adv. Water Resour. 122, 217–227. https://doi.org/10.1016/j.advwatres.2018.10.008.

Coceal, O., Belcher, S.E., 2004. A canopy model of mean winds through urban areas. Q. J. R. Meteorol. Soc. 130, 1349–1372. https://doi.org/10.1256/qj.03.40.

Dalrymple, R.A., Kirby, J.T., Hwang, P.A., 1984. Wave diffraction due to areas of energy dissipation. J. Waterw. Port, Coast. Ocean Eng. 110, 67–79. https://doi.org/10.1061/(ASCE)0733-950X(1984)110:1(67).

Davidson, K.E., Fowler, M.S., Skov, M.W., Doerr, S.H., Beaumont, N., Griffin, J.N., 2017. Livestock grazing alters multiple ecosystem properties and services in salt marshes: a meta-analysis. J. Appl. Ecol. 54, 1395–1405. https://doi.org/10.1111/1365-2664.12892.

Dean, R.G., Dalrymple, R.A., 1991. Water Wave Mechanics for Engineers and Scientists, Advanced Series on Ocean Mechanics. World Scientific Publishing Company, Singapore.

Dubi, A.M., 1997. Damping of Water Waves by Submerged Vegetation: A Case Study on Laminaria Hyperborea. (PhD Thesis). University of Trondheim, Trondheim, Norway.

Fagherazzi, S., Kirwan, M.L., Mudd, S.M., Guntenspergen, G.R., Temmerman, S., D'Alpaos, A., van de Koppel, J., Rybczyk, J.M., Reyes, E., Craft, C., Clough, J., 2012. Numerical models of salt marsh evolution: ecological, geomorphic, and climatic factors. Rev. Geophys. 50, RG1002 https://doi.org/10.1029/2011RG000359.

Feagin, R.A., Irish, J.L., Möller, I., Williams, A.M., Colón-Rivera, R.J., Mousavi, M.E., 2011. Short communication: engineering properties of wetland plants with application to wave attenuation. Coast. Eng. 58, 251–255. https://doi.org/10.1016/j.coastaleng.2010.10.003.

Foster, N.M., Hudson, M.D., Bray, S., Nicholls, R.J., 2013. Intertidal mudflat and saltmarsh conservation and sustainable use in the UK: a review. J. Environ. Manag. 126, 96–104. https://doi.org/10.1016/j.jenvman.2013.04.015.

French, J.R., 1993. Numerical simulation of vertical marsh growth and adjustment to accelerated sea-level rise, North Norfolk, U.K. Earth Surf. Process. Landforms 18, 63–81. https://doi.org/10.1002/esp.3290180105.

Garzon, J.L., Maza, M., Ferreira, C.M., Lara, J.L., Losada, I.J., 2019. Wave attenuation by Spartina saltmarshes in the chesapeake bay under storm surge conditions. J. Geophys. Res. Oceans 124, 5220–5243. https://doi.org/10.1029/2018JC014865.

Henderson, S.M., 2019. Motion of buoyant, flexible aquatic vegetation under waves: simple theoretical models and parameterization of wave dissipation. Coast. Eng. 152, 103497 https://doi.org/10.1016/j.coastaleng.2019.04.009.

Hu, Z., Suzuki, T., Zitman, T., Uittewaal, W., Stive, M., 2014. Laboratory study on wave dissipation by vegetation in combined current–wave flow. Coast. Eng. 88, 131–142. https://doi.org/10.1016/j.coastaleng.2014.02.009.

Jadhav, R.S., Chen, Q., Smith, J.M., 2013. Spectral distribution of wave energy dissipation by salt marsh vegetation. Coast. Eng. 77, 99–107. https://doi.org/10.1016/j.coastaleng.2013.02.013.

Keulegan, G.H., Carpenter, L.H., 1958. Forces on cylinders and plates in an oscillating fluid. J. Res. Natl. Bur. Stand. Res. Pap. 2857, 423–440.

Kobayashi, N., Raichle, A.W., Asano, T., 1993. Wave attenuation by vegetation. J. Waterw. Port, Coast. Ocean Eng. 119, 30–48. https://doi.org/10.1061/(ASCE)0733-950X(1993)119:1(30).

Koftis, T., Prinos, P., Stratigaki, V., 2013. Wave damping over artificial posidonia oceanica meadow: a large-scale experimental study. Coast. Eng. 73, 71–83. https://doi.org/10.1016/j.coastaleng.2012.10.007.

Lara, J.L., Maza, M., Ondiviela, B., Trinogga, J., Losada, I.J., Bouma, T.J., Gordejuela, N., 2016. Large-scale 3-D experiments of wave and current interaction with real vegetation. Part 1: guidelines for physical modeling. Coast. Eng. 107, 70–83. https://doi.org/10.1016/j.coastaleng.2015.09.012.

Le Méhauté, B., 1976. An Introduction to Hydrodynamics and Water Waves, first ed. Springer-Verlag, Berlin Heidelberg.

Leonardi, N., Carnacina, I., Donatelli, C., Ganju, N.K., Plater, A.J., Schuerch, M., Temmerman, S., 2018. Dynamic interactions between coastal storms and salt

marshes: a review. Geomorphology 301, 92–107. https://doi.org/10.1016/j.geomorph.2017.11.001.
Leonardi, N., Ganju, N.K., Fagherazzi, S., 2016. A linear relationship between wave power and erosion determines salt-marsh resilience to violent storms and hurricanes. Proc. Natl. Acad. Sci. Unit. States Am. 113, 64–68. https://doi.org/10.1073/pnas.1510095112.
Losada, I.J., Maza, M., Lara, J.L., 2016. A new formulation for vegetation-induced damping under combined waves and currents. Coast. Eng. 107, 1–13. https://doi.org/10.1016/j.coastaleng.2015.09.011.
Lowe, R.J., Koseff, J.R., Monismith, S.G., 2005. Oscillatory flow through submerged canopies: 1. Velocity structure. J. Geophys. Res. Oceans 110. https://doi.org/10.1029/2004JC002788.
Luhar, M., Coutu, S., Infantes, E., Fox, S., Nepf, H.M., 2010. Wave-induced velocities inside a model seagrass bed. J. Geophys. Res. Oceans 115. https://doi.org/10.1029/2010JC006345.
Luhar, M., Infantes, E., Nepf, H., 2017. Seagrass blade motion under waves and its impact on wave decay. J. Geophys. Res. Oceans 122, 3736–3752. https://doi.org/10.1002/2017JC012731.
Luhar, M., Nepf, H.M., 2016. Wave-induced dynamics of flexible blades. J. Fluid Struct. 61, 20–41. https://doi.org/10.1016/j.jfluidstructs.2015.11.007.
Luhar, M., Nepf, H.M., 2011. Flow-induced reconfiguration of buoyant and flexible aquatic vegetation. Limnol. Oceanogr. 56, 2003–2017. https://doi.org/10.4319/lo.2011.56.6.2003.
Maza, M., Lara, J.L., Losada, I.J., 2013. A coupled model of submerged vegetation under oscillatory flow using Navier–Stokes equations. Coast. Eng. 80, 16–34. https://doi.org/10.1016/j.coastaleng.2013.04.009.
Maza, M., Lara, J.L., Losada, I.J., Ondiviela, B., Trinogga, J., Bouma, T.J., 2015. Large-scale 3-D experiments of wave and current interaction with real vegetation. Part 2: experimental analysis. Coast. Eng. 106, 73–86. https://doi.org/10.1016/j.coastaleng.2015.09.010.
Mendez, F.J., Losada, I.J., 2004. An empirical model to estimate the propagation of random breaking and nonbreaking waves over vegetation fields. Coast. Eng. 51, 103–118. https://doi.org/10.1016/j.coastaleng.2003.11.003.
Méndez, F.J., Losada, I.J., Losada, M.A., 1999. Hydrodynamics induced by wind waves in a vegetation field. J. Geophys. Res. Oceans 104, 18383–18396. https://doi.org/10.1029/1999JC900119.
Miler, O., Albayrak, I., Nikora, V., O'Hare, M., 2012. Biomechanical properties of aquatic plants and their effects on plant–flow interactions in streams and rivers. Aquat. Sci. 74, 31–44. https://doi.org/10.1007/s00027-011-0188-5.
Möller, I., Kudella, M., Rupprecht, F., Spencer, T., Paul, M., van Wesenbeeck, B.K., Wolters, G., Jensen, K., Bouma, T.J., Miranda-Lange, M., Schimmels, S., 2014. Wave attenuation over coastal salt marshes under storm surge conditions. Nat. Geosci. 7, 727–731. https://doi.org/10.1038/ngeo2251.
Morison, J.R., Johnson, J.W., Schaaf, S.A., 1950. The force exerted by surface waves on piles. J. Petrol. Technol. 2, 149–154. https://doi.org/10.2118/950149-G.
Mork, M., 1996. Wave attenuation due to bottom vegetation. In: Grue, J., Gjevik, B., Weber, J.E. (Eds.), Waves and Nonlinear Processes in Hydrodynamics. Springer Netherlands, Dordrecht, pp. 371–382. https://doi.org/10.1007/978-94-009-0253-4_30.
Mullarney, J.C., Henderson, S.M., 2010. Wave-forced motion of submerged single-stem vegetation. J. Geophys. Res. Oceans 115. https://doi.org/10.1029/2010JC006448.
Nepf, H.M., 1999. Drag, turbulence, and diffusion in flow through emergent vegetation. Water Resour. Res. 35, 479–489. https://doi.org/10.1029/1998WR900069.
Nordstrom, K.F., 2014. Living with shore protection structures: a review. Estuar. Coast Shelf Sci. 150, 11–23. https://doi.org/10.1016/j.ecss.2013.11.003.
Ozeren, Y., Wren, D.G., Wu, W., 2014. Experimental investigation of wave attenuation through model and live vegetation. J. Waterw. Port, Coast. Ocean Eng. 140, 04014019 https://doi.org/10.1061/(ASCE)WW.1943-5460.0000251.
Paul, M., Henry, P.Y.T., Thomas, R.E., 2014. Geometrical and mechanical properties of four species of Northern European Brown macroalgae. Coast. Eng. 84, 73–80. https://doi.org/10.1016/j.coastaleng.2013.11.007.
Paul, M., Rupprecht, F., Möller, I., Bouma, T.J., Spencer, T., Kudella, M., Wolters, G., van Wesenbeeck, B.K., Jensen, K., Miranda-Lange, M., Schimmels, S., 2016. Plant stiffness and biomass as drivers for drag forces under extreme wave loading: a flume study on mimics. Coast. Eng. 117, 70–78. https://doi.org/10.1016/j.coastaleng.2016.07.004.
Phan, K.L., Stive, M.J.F., Zijlema, M., Truong, H.S., Aarninkhof, S.G.J., 2019. The effects of wave non-linearity on wave attenuation by vegetation. Coast. Eng. 147, 63–74. https://doi.org/10.1016/j.coastaleng.2019.01.004.
Price, W.A., Tomlinson, K.W., Hunt, J.N., 1968. The effect of artificial seaweed in promoting the build-up of beaches. In: Proceedings of 11th International Conference on Coastal Engineering, pp. 570–578. https://doi.org/10.1061/9780872620131.036.
Pujol, D., Serra, T., Colomer, J., Casamitjana, X., 2013. Flow structure in canopy models dominated by progressive waves. J. Hydrol. 486, 281–292. https://doi.org/10.1016/j.jhydrol.2013.01.024.
Riffe, K.C., Henderson, S.M., Mullarney, J.C., 2011. Wave dissipation by flexible vegetation. Geophys. Res. Lett. 38, L18607 https://doi.org/10.1029/2011GL048773.
Rupprecht, F., Möller, I., Paul, M., Kudella, M., Spencer, T., van Wesenbeeck, B.K., Wolters, G., Jensen, K., Bouma, T.J., Miranda-Lange, M., Schimmels, S., 2017. Vegetation-wave interactions in salt marshes under storm surge conditions. Ecol. Eng. 100, 301–315. https://doi.org/10.1016/j.ecoleng.2016.12.030.
Sánchez-González, J.F., Sánchez-Rojas, V., Memos, C.D., 2011. Wave attenuation due to Posidonia oceanica meadows. J. Hydraul. Res. 49, 503–514. https://doi.org/10.1080/00221686.2011.552464.
Stark, J., Plancke, Y., Ides, S., Meire, P., Temmerman, S., 2016. Coastal flood protection by a combined nature-based and engineering approach: modeling the effects of marsh geometry and surrounding dikes. Estuar. Coast Shelf Sci. 175, 34–45. https://doi.org/10.1016/j.ecss.2016.03.027.
Temmerman, S., Meire, P., Bouma, T.J., Herman, P.M.J., Ysebaert, T., De Vriend, H.J., 2013. Ecosystem-based coastal defence in the face of global change. Nature 504, 79–83. https://doi.org/10.1038/nature12859.
Vuik, V., Heo, H.Y.S., Zhu, Z., Borsje, B.W., Jonkman, S.N., 2018. Stem breakage of salt marsh vegetation under wave forcing: a field and model study. Estuar. Coast Shelf Sci. 200, 41–58. https://doi.org/10.1016/j.ecss.2017.09.028.
Vuik, V., Jonkman, S.N., Borsje, B.W., Suzuki, T., 2016. Nature-based flood protection: the efficiency of vegetated foreshores for reducing wave loads on coastal dikes. Coast. Eng. 116, 42–56. https://doi.org/10.1016/j.coastaleng.2016.06.001.
Wamsley, T.V., Cialone, M.A., Smith, J.M., Ebersole, B.A., Grzegorzewski, A.S., 2009. Influence of landscape restoration and degradation on storm surge and waves in southern Louisiana. Nat. Hazards 51, 207–224. https://doi.org/10.1007/s11069-009-9378-z.